



ÉCOLE NATIONALE SUPÉRIEURE DE PHYSIQUE ELECTRONIQUE ET
MATÉRIAUX
SIGNAL IMAGE COMMUNICATION ET MULTIMÉDIA

Master 2 Internship Report

Analysis of GNSS reflectometry data of the space mission TechDemoSat-1

Company Advisor : François Soulard
Academic Advisor : Jocelyn Chanussot

Internship done at :
Collecte Localisation Satellites
Division Océanographie Spatiale
11 Rue Hermès, 31520 Ramonville Saint-Agne

Ammar Mian
February - August 2016

Acknowledgements

I am grateful to my supervisor Francois Soulat, for his guidance through this internship. With his knowledge and assistance, this work has been made possible.

I would also like to thanks Tran Ngan for her help and input concerning the Chapter 5 of this thesis.

I thanks Dr Jocelyn Chanussot, my academic advisor, for following me and giving punctual advices to improve my work.

I am thankful to the IFREMER and peculiarly Alexis Mouché, for proving additional dataset used for the study.

I was fortunate to be in the Oceanography division of CLS, which was a pleasant place to work. I wish to thanks all my colleagues who made this stay enjoyable. The interns office was a great place for exchanging ideas. I am grateful to all the interns, who gave me helpful advices.

Contents

| | |
|--|-----------|
| Acknowledgements | 2 |
| Introduction | 8 |
| 1 Context of the internship | 10 |
| 1.1 Collecte Localisation Satellites | 10 |
| 1.2 Motivation of the Study | 10 |
| 1.3 Organisation of the Internship | 11 |
| 2 State of the art on GNSS signals Remote Sensing | 12 |
| 2.1 GNSS signals | 12 |
| 2.2 Sea surface Model | 13 |
| 2.2.1 Geophysical parameters involved | 14 |
| 2.2.2 Modelling the sea surface | 14 |
| 2.3 Geometry of the problem | 15 |
| 2.4 Scattering Model | 16 |
| 2.4.1 Kirchoff and GO approximations | 16 |
| 2.4.2 The Radar Equation | 18 |
| 2.4.3 The Delay Doppler Map | 19 |
| 2.4.4 The Waveform | 19 |
| 3 The TechDemoSat-1 mission | 21 |
| 3.1 Context of the spaceborne | 21 |
| 3.2 Data Product | 22 |
| 3.3 Data Coverage | 24 |
| 3.3.1 Time period | 25 |
| 3.3.2 Spatial coverage | 25 |
| 3.3.3 Storms co-localisation | 27 |
| 4 Implementation of a direct model using the Radar equation | 29 |
| 4.1 Coordinates system and Earth model | 29 |
| 4.2 Simulator specifications | 30 |
| 4.3 Computation of maps over the surface | 31 |
| 4.4 Results and Interpretation | 34 |
| 4.5 Conclusion | 43 |
| 5 Inversion of TechDemoSat-1 Waveforms | 44 |
| 5.1 General principle | 44 |
| 5.2 Co-localisation with WW3 and ASCAT | 45 |
| 5.3 Selection of TechDemoSat-1 Data | 47 |
| 5.3.1 Filters on Data | 47 |

| | | |
|--------------------|---|-----------|
| 5.3.2 | SNR as parameter from the waveform | 47 |
| 5.4 | First results of co-localisation | 49 |
| 5.5 | Regression using a model and least squares minimisation | 52 |
| 5.5.1 | Model and Optimisation problem | 52 |
| 5.5.2 | First results and performance | 53 |
| 5.5.3 | Weighted regression | 56 |
| 5.5.4 | Favourable case | 58 |
| Conclusions | | 61 |
| Résumé | | 64 |
| Abstract | | 64 |

List of Figures

| | | |
|------|--|----|
| 2.1 | Structure of GPS signals | 13 |
| 2.2 | Generation of GPS signals | 13 |
| 2.3 | Sea surface characteristics | 14 |
| 2.4 | Geometry of the problem | 15 |
| 2.5 | Back scattering over the sea surface | 16 |
| 2.6 | Geometric Optics approach | 17 |
| 2.7 | Configuration of delay and doppler areas | 19 |
| 2.8 | Interaction between the wave and the ocean surface in a Nadir case and with a high bandwidth | 20 |
| 2.9 | DDM waveform | 20 |
| 3.1 | (a) TDS-1 Satellite (b) SGR-ReSI instrument ©SSTL | 21 |
| 3.2 | Preliminary definition of TDS-1 GNSS-R Data Products ©SSTL | 23 |
| 3.3 | Example of track and data available. | 24 |
| 3.4 | Coverage of collection RD000001 (a) and RD000006 (b) | 26 |
| 3.5 | Example of repartition of land types | 27 |
| 3.6 | Flight over Nuri by TDS-1 | 28 |
| 4.1 | ECEF coordinates versus the SP centred system | 30 |
| 4.2 | Organisation of the simulator | 30 |
| 4.3 | Example of σ_0 (dB) generated over the surface. Units are in meters. | 32 |
| 4.4 | (a) Delay Map (b) Doppler Map for RD000003 track 11 at 2014-10-06T11:52:21.4567692 | 33 |
| 4.5 | Antenna Gain (dB) for RD000003 track 11 at 2014-10-06T11:52:21.4567692 | 34 |
| 4.6 | Simulated DMM and delay waveform for RD000006 track 191 at 2014-10-31T12:00:13.9714486 | 35 |
| 4.7 | DMMs for RD000001 track 7 2014-09-01T10:48:19.4973256 | 36 |
| 4.8 | DMMs for RD000002 track 1 at 2014-09-01T20:11:05.8811101 | 37 |
| 4.9 | DMMs for RD000001 track 10 at 2014-09-01T10:56:16.4982748 | 37 |
| 4.10 | 1D waveform for the case of specular reflection vs non specular | 38 |
| 4.11 | Power for several wind speed in a specular situation | 39 |
| 4.12 | Waveform simulated for different winds speed for RD000004 track 0 at 2014-10-14T21:48:11.9772487 | 39 |
| 4.13 | Waveform simulated (Doppler 0) for different winds speed for RD000004 track 0 at 2014-10-14T21:48:11.9772487 | 40 |
| 4.14 | Waveform simulated for different winds speed for RD000006 track 191 at 2014-10-31T12:00:13.9714486 | 41 |
| 4.15 | Waveform simulated (Doppler 0) for different elevations for RD000006 track 191 | 42 |
| 4.16 | Waveform measured (Doppler 0) for different elevations for RD000006 track 191 | 42 |

| | | |
|------|---|----|
| 5.1 | Example of global U10 ($m.s^{-1}$) map provided by WW3 at 30/12/2012 12:00::00 | 45 |
| 5.2 | Histogram of ASCAT and WW3 wind | 46 |
| 5.3 | Example of computation of SNR | 48 |
| 5.4 | Probability of mistake for different sizes of Gaussian Kernel | 49 |
| 5.5 | SNR(U10) | 50 |
| 5.6 | SNR(U10) after cleaning | 50 |
| 5.7 | SNR(U10, e) | 51 |
| 5.8 | Mean SNR(U10, e) | 51 |
| 5.9 | Results of the regression on the test set for range 60 - 90 | 54 |
| 5.10 | Results of the regression on the test set for range 70 - 90 | 54 |
| 5.11 | Results of the regression on the test set for range 80 - 90 | 55 |
| 5.12 | Histogram of the wind Ww3 | 55 |
| 5.13 | Weighted regression $w(U10 >10) = 0.6$ $w(U10 >12) = 0.4$ $w(U10 >15) = 0.1$ | 57 |
| 5.14 | U10 TDS-1 vs U10 WW3 by range of SWH (m) | 58 |
| 5.15 | Exponential regression Favourable case | 59 |
| 5.16 | Exponential regression Favourable case and weights | 60 |

List of Tables

| | | |
|-----|--|----|
| 3.1 | Characteristics of TDS-1 | 22 |
| 3.2 | Dates and duration of data by collection | 25 |
| 4.1 | Common parameters for Waveforms simulation | 35 |
| 5.1 | ASCAT vs WW3 | 46 |
| 5.2 | Number of points by range of elevation | 53 |
| 5.3 | Results of Regression with exponential model | 53 |
| 5.4 | Results of Regression with logarithm model | 53 |
| 5.5 | Bias and variance by range of wind | 56 |
| 5.6 | Results of regression with weights | 56 |
| 5.7 | Results by range of SWH and considering points for which $U_{10} > 15m.s^{-1}$ | 58 |
| 5.8 | Results of the regression in a Favourable case | 59 |
| 5.9 | Results of the regression in a Favourable case with weights | 60 |

Introduction

The six months internship at the end of the third year is the opportunity to have a valuable experience in a company. It allows to work in a domain of interest and deepen one's knowledge of a subject. I chose to do an internship at CLS (Collecte Localisation Satellites) in the domain of Remote sensing applications to Oceanography.

CLS is a subsidiary of the CNES which aims at providing satellite systems and high value-added services. Typical applications are environmental monitoring, sustainable management of marine resources, and maritime security.

In this context, arises the problem of the retrieval of oceanographic data, which is a key component in modern meteorological analysing and forecasting, as well as a resource for climate research. For a time, the lack of measurements was a problem as methods such as buoys, planes or boats were not efficient in the retrieval of numerous datasets. But with the development of remote-sensing instruments such as scatterometers or synthetic aperture radars, it is now possible to obtain a large quantity of data.

In the past few years, an original Remote Sensing concept, which focuses on passive retrieval of oceanographic data through reflections of GNSS (Global Navigation Satellite Systems) signals, has been developed. The instrument is passive as it does not emit any signal itself and only receives radio waves. The principle is then to use these reflected signals that have interacted with the sea surface as a geophysical signature and try to infer properties of the reflecting surface.

The focus of this internship is to study the data of a recently launched mission TechDemoSat-1 in this context of GNSS-R (GNSS Reflectometry) for sea-state retrieval at global scale. The satellite carries a GPS receiver which allows the reception of L-band signals ($\sim 20\text{cm}$), a first level of processing and their transmission on ground for post-processing. The internship's objectives are to develop applications for visualising and processing the data, understand the physical interactions and develop methods for the retrieval of geophysical quantities.

This thesis aims at presenting the complex problematic underlying this type of remote-sensing technique as well as the work I've done during these six months and the results I have obtained. The organisation of the thesis is as follows.

The first chapter will develop the context in which I have done my internship, including a description of the company and its motivations for the current work. Chapter 2 is a state of the art on the GNSS-R. It starts with a brief remainder of the characteristics of a GNSS signal and ways to detect and process them. We then describe the geophysical quantities which will be the aim of our retrieval algorithms, the geometry of the problem and a model of the interactions between the sea surface and radio waves with the corresponding physical assumptions. Chapter 3 will be focused on describing the TechDemoSat-1 mission. It will give the context and the characteristics of the instrument and its coverage. Chapter 4 presents the implementation of a direct model with

the radar equation. It develops the assumptions and methods used as well as the choices for the implementation. Chapter 5 is the main contribution of this thesis as it presents methods developed to retrieve geophysical data from the TechDemoSat-1 dataset and the results obtained.

Chapter 1

Context of the internship

1.1 Collecte Localisation Satellites

CLS (Collecte Localisation Satellites) is a subsidiary of the CNES (Centres National d'Etudes Spatiales), IFREMER (Institut Francais de Recherche pour l'Exploitation de la MER) and the investment firm ARDIAN.

It has been operating satellite systems and providing high value-added products and services since 1986. Each day, CLS provides operational services for environmental monitoring, sustainable management of marine resources, and maritime security. The company also provides services for telematics. Through its range of products and services, CLS provides direct operational assistance to stakeholders in both the public and private sectors. CLS operates over 80 instruments carried by 40 satellites and provides its expertise to a broad range of customers: governments, scientific organizations, non-governmental organizations, institutions, large industrial groups (maritime freight, oil and gas companies, commercial shipping, fisheries, etc).¹

During my internship, I was a part of the DOS (Division Oceanographie Spatiale) under the supervision of Francois Soulard. The DOS division has the mission to carry out studies and develop methods in order to process and validate remote sensing data. The purpose is to monitor, model and predict the behaviour of oceans, marine ecosystems and hydrologic resources. My team was the IPM (Instrumentation et Physique de la Mesure) which is focused in processing and validating coming from captors.

1.2 Motivation of the Study

The main focus of the internship was to analyse the dataset of a recent space mission, TechDemoSat-1. This mission is particularly interesting as it uses a recent Remote sensing technique called the GNSS-R. It consists of using the reflections of the GPS signals over the ocean surface as a source of opportunity in order to measure geophysical data.

This technique is interesting for the scientific community as it offers a strong potential in terms of space and time coverage with a low cost technology. Indeed, as the GPS signals are emitted in permanence, only an antenna to receive them is needed.

The second contribution of this technique is the use of a large wavelength, which is in theory not impacted by rain cells or clouds. This is interesting if we want to study

¹Description taken from <https://www.cls.fr/en/cls-group/>

storms as it could allow to measure geophysical data for places unavailable before. This is the peculiar objective that was in mind for the internship. The geophysical data of interest is then the surface wind speed and will be the focus of the study.

1.3 Organisation of the Internship

The internship was decomposed in the following steps :

- Study of the bibliography about GNSS-R techniques in order to grasp the subject. This was a needed step in order to comprehend the geometry of the problem and the geophysical quantities that play a role. This step lasted a month.
- Development of tools in order to visualise and treat the dataset. Indispensable for the study, it first consisted on developing python scripts to read the dataset and then to characterise the dataset in term of coverage. It lasted about 2 months.
- Implementation of a model. For the purpose of understanding the signals scattered from the ocean's surface, a model was developed according to the work presented in [Zavorotny and Voronovich, 2000]. This step lasted about a month.
- Inversion of the dataset. It consisted of developing methods to invert the dataset in order to retrieve the wind speed. It took about a month and a half.

The organisation of the thesis follows the different steps in the same order.

Chapter 2

State of the art on GNSS signals Remote Sensing

This chapter describes fundamentals notions used in GNSS-R and the remainder of this thesis. It presents the geophysical quantities of interest, as well as the physical theory which is necessary to understand the signals we will process, and the assumptions we make in order to develop retrieval methods. First, we present the characteristics of the signals that are emitted, then we describe the ocean surface on which these signals will be reflected and we finally present a model for the interaction between the electromagnetic waves and the surface.

2.1 GNSS signals

GNSS - Global Navigation Satellite System - is a technology designed to provide, for any point on the surface of the Earth, a capability of navigation by giving position and speed of an object. GPS (Global Positioning System), the first system using this technology, was put in place by the United States in the seventies. It consists of a constellation of 24 satellites in 6 different planes at an altitude of about 20200 km.

We can find in [Zavorotny et al., 2014], a thorough description of the GPS signal structure. In short, the GPS signal is structured using spread spectrum techniques. It consists of spreading the bandwidth of a navigation signal by mixing it with a pseudo-random rectangular signal sequence, the PRN (Pseudo-Random Noise) which is at much higher frequency than the data. The PRN acts as an identifier of the GPS satellite that emits, as it is deterministic and have an auto-correlation similar to a Gaussian noise.

The goal of this spreading is to have a lower power spectral density to avoid interferences with other systems, in addition to the multiple access capabilities.

The data signal is a bi-phase modulation with a symbol rate of 50 Hz. It provides the user with information such as ephemeris or almanacs. For the PRN, two types of signal are used : The C/A (Coarse/Acquisition), which is aimed at civil applications, and the P (Precise) that is used by the military. The C/A code has a rate of 1.023 MHz when the P has a rate of 10.23 MHz.

The whole signal is then put on two different carriers L1 and L2 for transmission. The wavelength used lays in L-band which allows to avoid rain effects. The figure 2.1 illustrates the combinations used for the two different carriers.

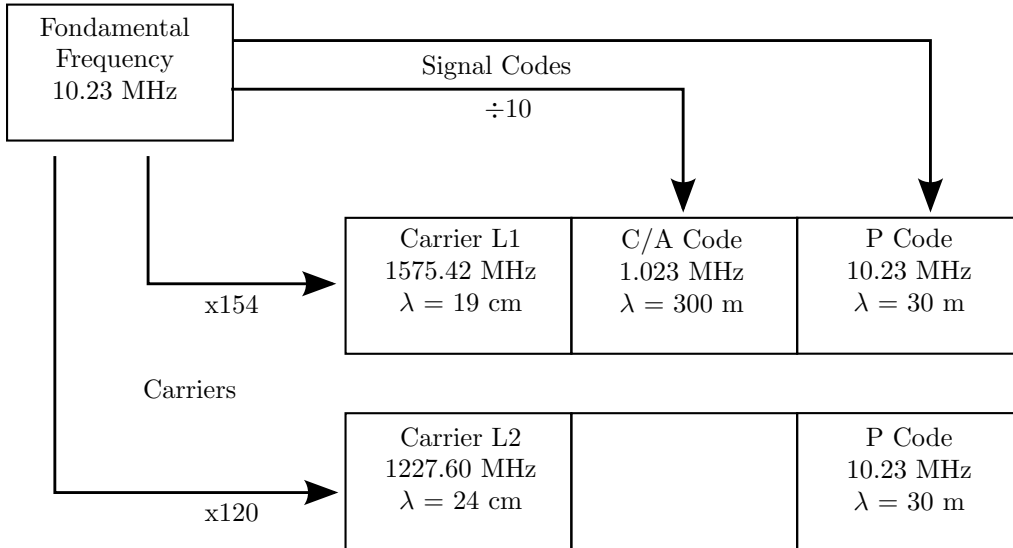


Figure 2.1: Structure of GPS signals

For the application of GNSS-R, L1 carrier is used as P code is unknown and informations about ephemeris and almanacs are not available. The process of generating these signals can be summarised by the figure 2.2.

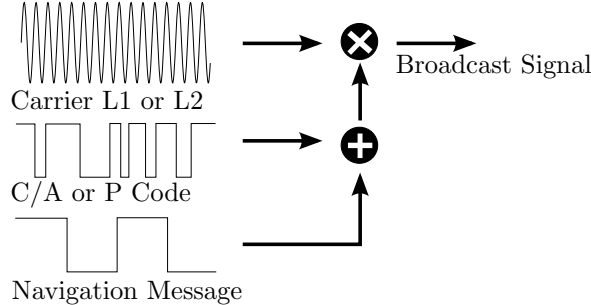


Figure 2.2: Generation of GPS signals

The detection of GPS signal can be done by searching a replica of C/A PRN into several Doppler frequencies and delays to find a correlation peak. Once the peak is found, the receiver is able to decode the navigation message as it can track the C/A code.

2.2 Sea surface Model

The sea is a complex system whose shape is dependant on a great number of geophysical parameters. This section aims at providing a simple model for its representation with limited geophysical parameters involved. This model will be useful for developing a model for the wave matter interaction between the GNSS signals and the sea.

2.2.1 Geophysical parameters involved

The sea state is the condition of a large body of water , with respect to the wind and the swell, at a certain location in time and space. It can be approximated as a two dimensional wave which varies with time as the wind and swell conditions change.

The wind is an essential factor that plays on the surface roughness. The geophysical quantities used in oceanography are the following :

- U10 is the wind speed measured (in $m.s^{-1}$) at ten meters over the surface. The 10 meters height is chosen as to avoid the boundary layer in which the air has a turbulent behaviour.
- The direction of the wind is given in azimuth degrees (degrees in axis East-North).

The wave is then characterized by several statistics such as :

- Sea-surface height (SSH) corresponds to the mean of the ocean surface's height.
- The significant wave height (SWH or hs) corresponds to four times the standard deviation of the surface height. It is used to measure the height of the surface waves.
- The mean square slope (MSS) corresponds to the average of the local slopes. It is dependent to the first order on the wind.

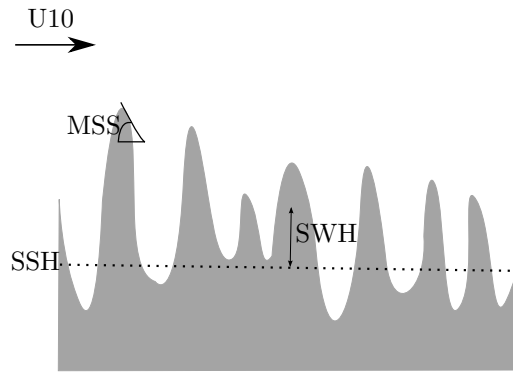


Figure 2.3: Sea surface characteristics

2.2.2 Modelling the sea surface

Many attempts have been made in order to model the ocean's surface. [Soulat, 2003] gives an overview of means to generate a sea surface using different spectra. It presents in particular the work of [Elfouhaily et al., 1997], which is the model most popular in the Oceanography community.

We will not describe these models here, but we can give the following conclusions :

- There is no accepted description of the wave spectrum
- [Elfouhaily et al., 1997] seems the best available although it has some shortcomings.
- There are a lot of phenomena affected by Wave breaking, currents or rain that are yet to be explained.

The task of having a solid representation of the sea state seems to be a complex one. We will for the purpose of this thesis make the following assumptions. The surface is represented by the height of the surface $\zeta = \zeta(x, y)$ and has a Gaussian distribution. It can be shown [Soulat, 2003], that if the sea height is Gaussian, then the distribution of the slopes is also Gaussian. And we can express the pdf of this distribution by :

$$P_s(s_x, s_y) = \frac{1}{2\pi\sqrt{\det(M)}} \exp \left[-\frac{1}{2} \begin{pmatrix} s_x \\ s_y \end{pmatrix}^T M^{-1} \begin{pmatrix} s_x \\ s_y \end{pmatrix} \right] \quad (2.1)$$

where $s_x = \frac{\partial \zeta}{\partial x}$ and $s_y = \frac{\partial \zeta}{\partial y}$ are the directional slopes in some frame xy and M, the matrix of slope second order moments given by :

$$M = \begin{bmatrix} \cos\psi & -\sin\psi \\ \sin\psi & \cos\psi \end{bmatrix} \cdot \begin{bmatrix} \sigma_u^2 & 0 \\ 0 & \sigma_c^2 \end{bmatrix} \cdot \begin{bmatrix} \cos\psi & \sin\psi \\ -\sin\psi & \cos\psi \end{bmatrix} \quad (2.2)$$

σ_u^2 , σ_c^2 , ψ are the geophysical parameters : ψ stands for the angle between the x axis and the principal direction of the slope, σ_u^2 stands for the MSS along the slope direction (MSS up-wind) and σ_c^2 for the MSS in the direction at 90° (MSS cross-wind). The total MSS can be retrieved by $MSS = 2\sqrt{\sigma_u^2 \cdot \sigma_c^2}$.

2.3 Geometry of the problem

As said in the Introduction, the GNSS-R is a bistatic problem as the satellite that transmits the radio wave and the one receiving it is not the same. We give here a formal definition of the geometry and the terminology used. The figure 2.4 describes the geometry and the reference frame used.

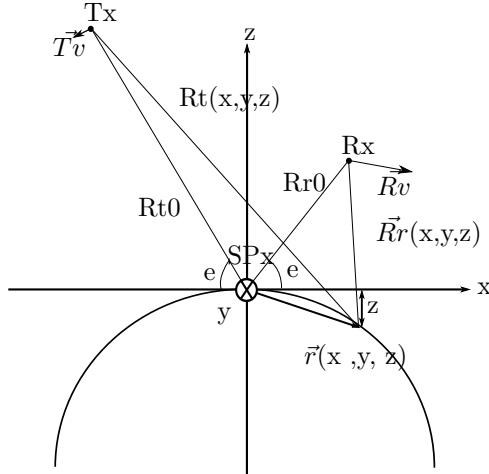


Figure 2.4: Geometry of the problem

The geometry is the following :

- **Rx** corresponds to the satellite receiving the radio wave reflected and **Tx** corresponds to the GPS satellite that transmits the wave. **Rv** and **Tv** are the respective velocities of Rx and Tx.
- **SPx** is the specular point. It is the point of the surface that has the minimum distance ($Rt_0 + Rr_0$). It is used as the center of the reference frame (xyz).

- ϵ is the elevation angle, it corresponds to the angle between the surface at SPx and the line between SPx and Rx. It is an important quantity which plays an important part on the quality of the signal obtained.

2.4 Scattering Model

The GNSS signals illuminating the Ocean will interact with its surface through a wave matter interaction. The signatures of oceanic features that we want to detect results from the interaction between the electromagnetic waves and the water waves. It is then necessary to have a picture of the physical process involved in the electromagnetic ocean-surface interaction in order to extract these features.

We can find detailed descriptions of such interactions at L band in a bistatic context in [Elfouhaily et al., 2002], [Soulat, 2003] or in [Zavorotny et al., 2014], which describes in our context the physical interactions that have to be taken into account. We will not here describe all the physical phenomena that can be taken into account, but rather give the essential assumptions and develop a model of the signals received at the Receiver Satellite based on the assumptions and the model of sea surface developed in 2.2.

2.4.1 Kirchoff and GO approximations

The electromagnetic waves emitted by the GPS satellites will propagate through the Earth's atmosphere in which there is not much interaction between the waves and the air molecules given the wavelength. Then, upon meeting with the sea surface, they will interact through a scattering phenomenon. The sea will scatter the electromagnetic waves that can reach the receiver. The capacity for the sea surface to scatter power back towards the receiver is characterised by the NCRS (Normalised Cross Radar Section) or σ_0 . This concept is illustrated in figure 2.5. If the sea surface is smooth, the backscattering is specular and the wave is reflected as in geometric optics in the Specular direction. But in most of the cases, the surface presents some roughness and the back scattering is quasi-specular, the σ_0 in dB quantifies that.

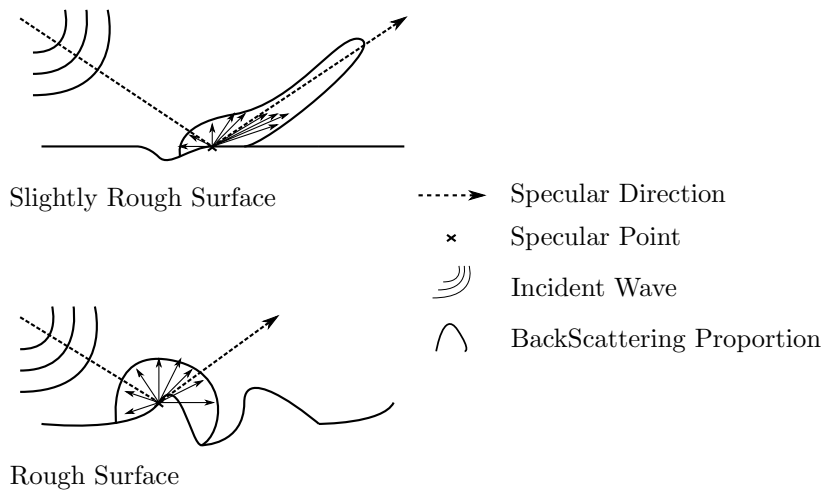


Figure 2.5: Back scattering over the sea surface

The GNSS signals scattered on the ocean surface are generally weak, so it is challenging to acquire such signals. This results that in practice, signals received by GNSS

radars comes from the scattering of limited zone around the Specular Point as in the figure 2.4. This zone is called the "Glistening Zone" and its size depends on the wavelength of the wave emitted, the elevation angle and the local characteristics of the ocean. The signals received are then obtained by reflections inside the glistening zone. To represent this phenomenon we use the KA (Kirchoff Approximation) and GO (Geometric Optics) approximations.

The Kirchoff Approximation is one of the most widely used assumption. It states that the surface is smooth enough to be locally represented by planes. It is an approximation of the exact solution of the Stratton-Chu equations [Stratton, 1941] for the electromagnetic fields scattered from a surface and allows to simplify the problem. The requirement for this approximation relies on the radius of curvature of the surface r_c and the following condition :

$$2kr_c \cos(\pi - e) \gg 1 \quad (2.3)$$

where k is the wave number of the incident wave and e is the elevation angle. This condition means that the local radius of curvature is much larger than the wavelength of the indent wave, so that we can consider it as a plane.

At this approximation we can add another assumption which is the GO (Geometric Optics). It means, physically, that the electromagnetic field at the point of reception is determined by the contributions from a multitude of points distributed over a portion of the rough surface. We can see it as the following analogy :

The sea surface is composed of a multitudes of tiny mirrors called facets, the signal received is then the sum of the waves reflected by the mirrors that were in the right inclination to reflect the wave in the direction of the receiver (see figure 2.6 for an illustration). The phenomenon can then be viewed globally as a specular reflection as in geometrics optics.

We can find a validation of this assumption at L band in [Soulat, 2003].

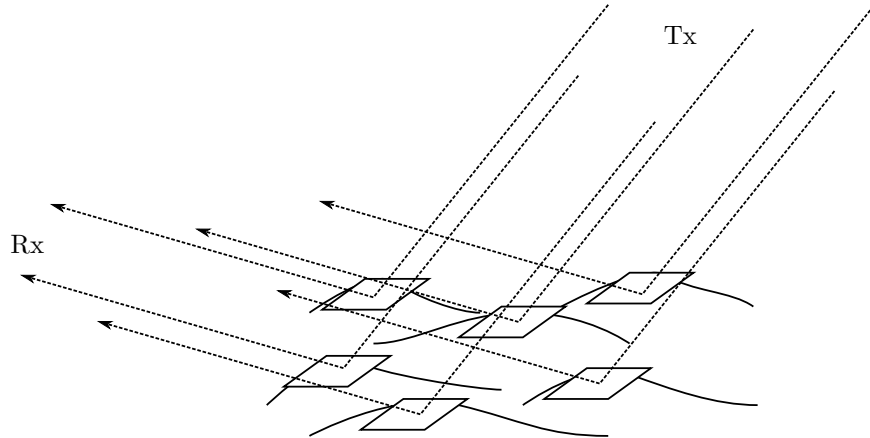


Figure 2.6: Geometric Optics approach

2.4.2 The Radar Equation

The receiver satellites have typically two antennas :

- The Nadir antenna which is pointed at the nadir of the satellite, which means directly pointed downwards with respect to the earth vertical direction at the location of the satellite. This antenna will receive the GNSS signals back scattered from the ocean's surface.
- The Zenith antenna which is pointed at the opposite of the Nadir antenna. This antenna will receive the GNSS signals transmitted by the GPS satellite directly, without any scattering.

After scattering from the rough surface, the waves are received by the antenna on the receiver satellite. The signal is then correlated with the direct signal received from the Zenith antenna. If we take t_0 as the time at which the direct signal u is received, we have :

$$Y(t_0, \tau) = \int_0^{T_i} A u(t_0 + t') u(t_0 + t_{off} + \tau + t') \exp(2\pi f_c t') dt' \quad (2.4)$$

T_i is the coherent integration time which is much larger than the duration of a GNSS frame and much shorter than the period of the PRN.

t_{off} accounts for the time offset between the direct and the reflected signal

f_c is aimed at compensating a possible Doppler Shift of the signals because of the movement of the satellite.

Conventionally, in GPS applications, this procedure is used to find t_{off} by searching for the maximum of the correlation in delay and doppler. There is no direct signal and a replica of the PRN is used. The code is then demodulated and the signal becomes "despread".

For the scattering of GNSS signals on the Earth's surface, we suppose that the surface is frozen during the time of integration T_i .

We can rewrite that integral and show [Zavorotny and Voronovich, 2000] that the mean of the correlation power can be expressed for any delay and doppler shift by the following :

$$\langle |Y(\tau, f)|^2 \rangle = \frac{\lambda^2 T_i^2}{(4\pi)^3} P_t G_t \iint_S \frac{G_r}{R_t^2 R_r^2} \chi^2(\tau, f) \sigma_0 dS \quad (2.5)$$

where :

- T_i is the coherent integration time
- $P_t G_t$ is the transmitter's effective radiated power
- G_r is the receiver antenna gain pattern
- R_t and R_r are the distances between the point on the surface and the transmitter/receiver as in the figure 2.4
- χ^2 is the WAF (Woodward Ambiguity Function)
- σ_0 is the normalised radar cross section
- S is the surface illuminated by the wave

The WAF is the product of a triangle function and a cardinal sinus :

$$\begin{aligned}\chi(\tau, f) &= \Lambda(\tau).S(f) \\ S(f) &= \text{sinc}(\pi f T_i) \exp(-i\pi f T_i) \\ \Lambda(\tau) &= 1 - |\tau|/\tau_c, |\tau| \leq \tau_c(1 + \frac{\tau_c}{T_i})\end{aligned}\quad (2.6)$$

τ_c being the duration of a chip of the information signal. This function describes the range and doppler selectivity of the radar.

2.4.3 The Delay Doppler Map

For the purpose of using the equation 2.5, we can map the glistening zone in term of delay and doppler. Indeed, during the time of coherent integration we suppose that the surface is frozen. Then, for each point of the glistening we can associate a delay and a doppler shift and have subsequently a DDM (Delay Doppler Map) of the surface.

The delay at a given point $\vec{r} = (x, y, z)$ is given by $\tau = \frac{R_t + R_r}{c}$ and the doppler shift is given by $f_D = [\vec{T}_v \cdot \vec{m}(\vec{r}, t_0) - \vec{R}_v \cdot \vec{n}(\vec{r}, t_0)]/\lambda$ where \vec{m} is the unit vector of the incident wave and \vec{n} is the unit vector of the scattered wave.

The areas at the same delay are the isoDelays and describe ellipsoids on the surface. The areas at the same doppler are the isoDopplers and describe hyperboloids. The figure 2.7 illustrates the mapping of the surface for a DDM with a given resolution in Doppler and Delay. The areas delimited by the intersection of isoDoppler and isoDelay corresponds to a pixel of the DDM. We can also note that for a given pixel, we can usually find two areas corresponding which introduce a right/left ambiguity with respect to the SP track.

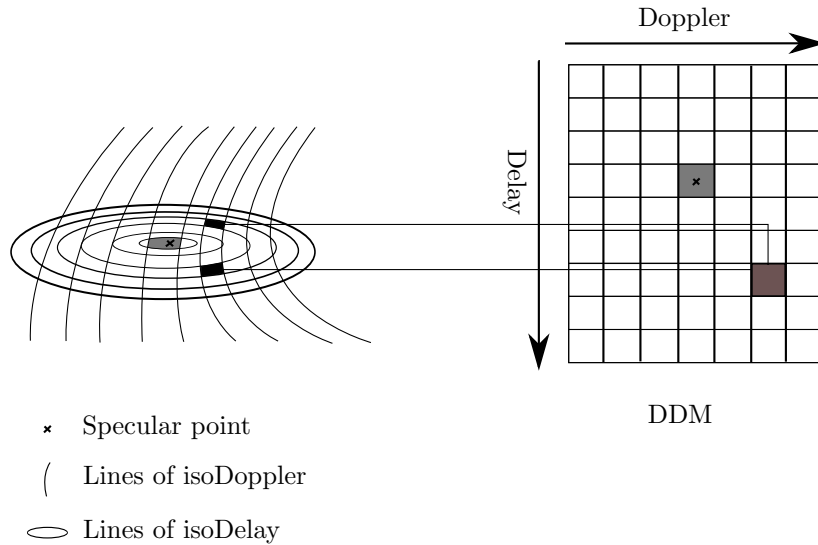


Figure 2.7: Configuration of delay and doppler areas

2.4.4 The Waveform

The power received from the reflection of the waves on the ocean's surface is called the waveform. Its form is well described physically in [Amarouche, 2001].

If we look at the radar equation (cf equation 2.5), the power received is dependent on the area of the surface that was illuminated by the wave. The first signal received comes from the peak of the ocean's waves. The electromagnetic wave will then penetrate the ocean's surface and the area illuminated will grow linearly with time. When the electromagnetic wave will reach the bottom of the ocean's waves, the area illuminated will take the form of a ring of constant area. The power received will then remain constant or diminish because the viewing angle will be larger and the transmitter's antenna gain diminish with the viewing angle.

This process is summarised by figure 2.8. The figure presents the form of the power received as a function of delay for the different phases of the interaction.

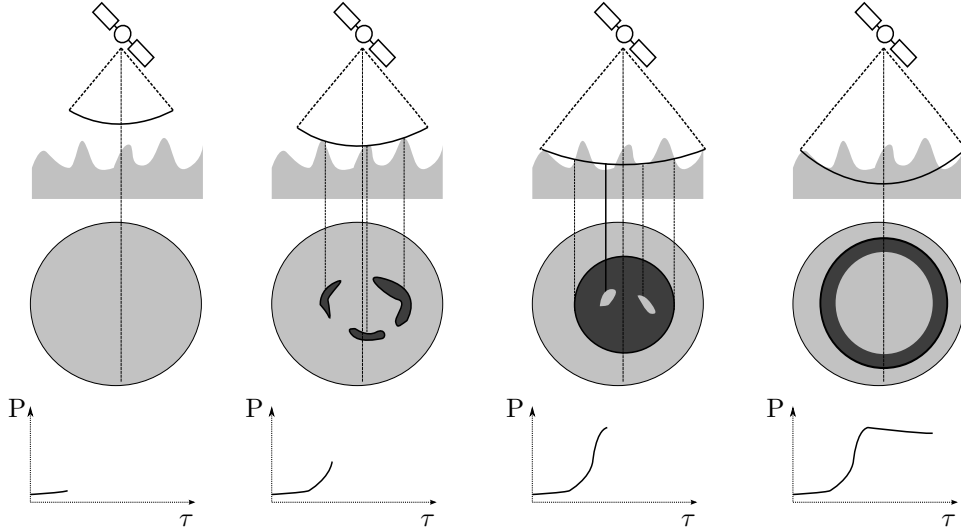


Figure 2.8: Interaction between the wave and the ocean surface in a Nadir case and with a high bandwidth

If we look at the waveform through the decomposition in Delay Doppler Map, it gives the form presented in figure 2.9. The form is easily explained by the fact that when the doppler shift difference from the one at SPx augments in absolute value, the area on the surface corresponding to the doppler is further away from the specular point. This introduce an additional delay for the power received in these zones.

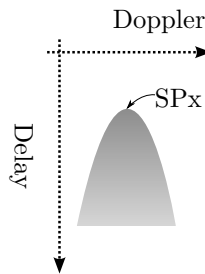


Figure 2.9: DDM waveform

This waveform is used to infer geophysical quantities. It is indeed shown [Amarouche, 2001], that the peak of the waveform is linked with the σ_0 which is a quantity of interest for the wind.

Chapter 3

The TechDemoSat-1 mission

The first step in the internship was to explore the data available for our study and develop tools for analysing and treating the raw data. In this chapter, we describe the TDS-1 (TechDemoSat-1) mission, the context in which it was launched and its specifications. We then describe the products available for our study and the coverage of the dataset.

3.1 Context of the spaceborne

In the context of examining the Remote Sensing capabilities of the GNSS-R technology, campaigns for acquiring data have been launched. The TDS-1 mission is a mission following the UK-DMC experiment¹ which demonstrated feasibility for both ice and soil moisture measurements combined with the ocean state sensing capability from a low cost experiment[Gleason et al., 2005].

To further develop sensing capabilities, the technology demonstration satellite, TDS-1 (TDS-1) mission was put in place. The satellite has been developed in the UK under sponsorship of the UK Space Agency and Innovate UK (Technology Strategy Board) and with contributions from the payload suppliers. TDS-1 was launched from Baikonur Cosmodrome on a Soyuz-2 launcher on 8th July 2014.

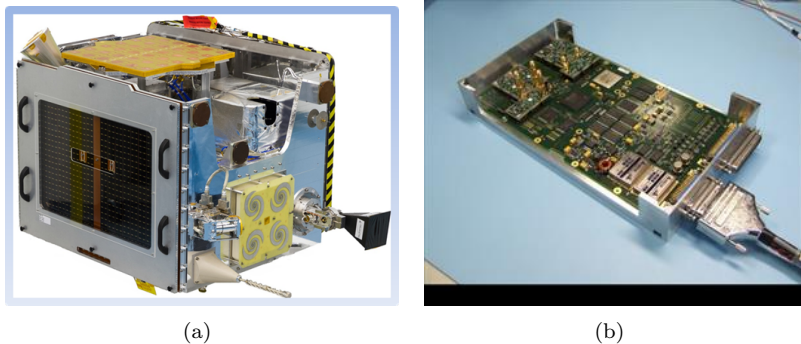


Figure 3.1: (a) TDS-1 Satellite (b) SGR-ReSI instrument ©SSTL

¹ see <https://www.sstl.co.uk/Missions/UK-DMC-1-Launched-2003/UK-DMC-1/UK-DMC-1-The-Mission>

The satellite carries on-board an enhanced Remote Sensing Instrument from the UK-DMC named SGR-ReSI, which was designed specifically for GNSS-R. It can process GPS signals on-board to compute DDMs and send them back to Earth for analysis. The satellites characteristics and GPS capabilities are presented in table 3.1.

| Geometry | |
|---------------------------|--------------|
| Altitude | ~ 620 km |
| Speed | ~ 7 km/s |
| GPS | |
| Frequency | L1 and L2C |
| Wavelength | ~ 19 cm |
| Nadir Antenna Gain | 13 dBi |
| Channels | 4 |
| Processing | |
| Coherent Integration Time | 1 ms |
| Incoherent Integration | 1000 samples |
| Gain Mode | Automatic |

Table 3.1: Characteristics of TDS-1

Using these specifications, we can roughly estimate the spatial resolution of the instrument on the surface. The Doppler resolution (distance between two hyperbolas) for a radar is given by :

$$R_{Dop} = \frac{\lambda H}{2vTi} \quad (3.1)$$

with $Ti = 1ms$. The waveform are then averaged on 1000 samples do diminish the interference of the waves (also known as speckle phenomenon). It gives here a resolution of about 10 km. The Delay resolution (distance between two ellipsoids) can be roughly estimated to 1 km. We must keep in mind that the resolutions are dependent of the elevation angle as the geometry is bistatic.

The resolutions obtained are relatively low, which is to be expected given the wavelength, the bandwidth and the integration time used. By means of classical methods, it is thus not possible to have a local measurement using this technology but rather a mean on a surface of 100 km.

The SGR-ReSI possesses four channels, which means that it can process signals coming from four different GPS transmitters at the same time. Indeed, as the satellite orbits, it receives reflections from a great number of satellites and choose the four best, in terms of elevation angle and power received, for processing the DDMs. This allows to collect a large dataset in a shorter period of time, or in other words, to mimic a swath type of measurement.

3.2 Data Product

The products in the Oceanography domain are labelled according to the nature of the data. The categories of products go from raw data received by the satellite to geophysical quantities or meteorological maps. The figure 3.2 illustrates the different kind of data available and its categorisation.

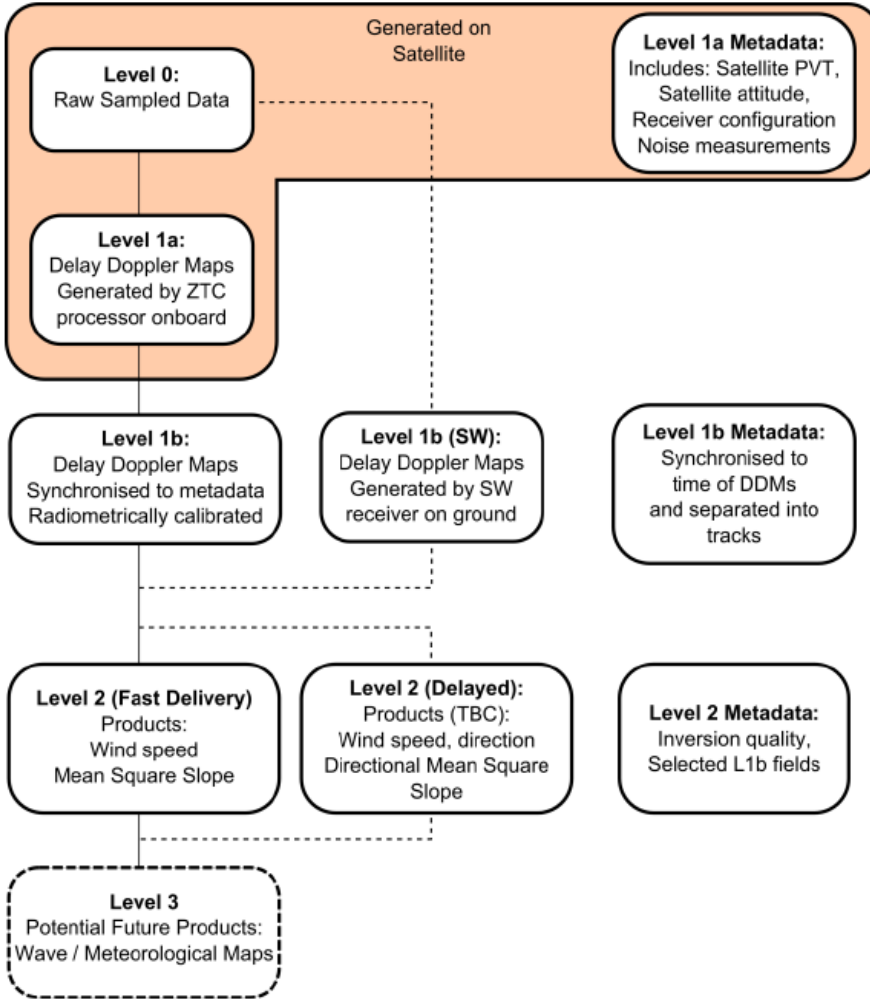


Figure 3.2: Preliminary definition of TDS-1 GNSS-R Data Products ©SSTL

The current study is based on the Level 1b data which contains Delay Doppler Maps computed from the raw data and additional metadata which corresponds to the positions, velocities of satellites, time stamp and other relevant quantities. It is organised as such :

- Dataset are separated by periods of time in collections which are named RD0000xx, xx being the collection number.
- Each collection contains several tracks which are a continuous series of DDMs from the same GPS transmitter. The figure 3.3 presents an example of ground track, the red line corresponding to a succession of specular points which are the localisation of the reflection of GPS signals.
- For each track we have access to a succession of waveforms. Additionally, for each waveform, we have access to the metadata which contains informations about the geometry (positions and velocities of satellites), timestamps in UTC format (i.e 2014-10-31T12:00:13.9714486), and various informations about the receiver satellite status.

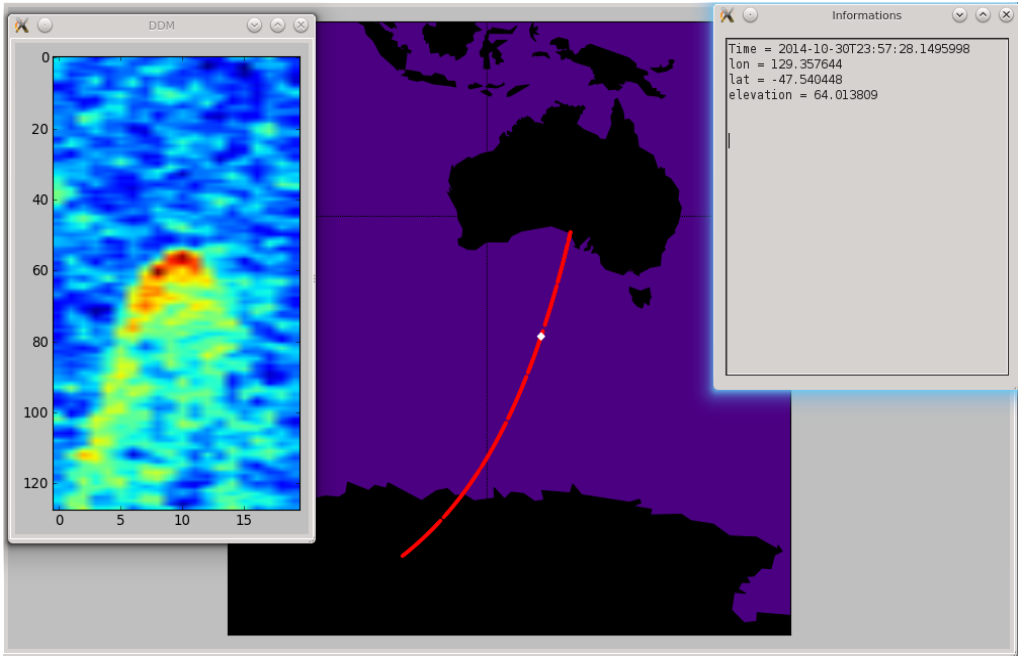


Figure 3.3: Example of track and data available.

The metadata is contained in several xml files and the waveform are stored in tiff image format. Both are indexed by the time of the integration of the DDM. A considerable amount of time was devoted to develop means of visualising and process this data. Several scripts were designed to find all the data at a given time, which was disseminated in several files, in the most convenient and optimal manner. They are essentially based on the lxml library of Python which has several methods convenient to parse and search in xml files. Figure 3.3 gives an example of an application developed in order to visualise the successions of DDMs along a track and have informations about the geometry.

Along with this dataset, we have access to the characteristics of the satellite such as the antenna gain as an array indexed by elevation and azimuth from the satellite reference frame.

The organisation of the dataset gives an elegant way of processing large quantities of data. The detailed characteristics make it possible to understand the physical interactions and the processing done in order to obtain the DDMs. This proves to be useful when trying to invert the data.

3.3 Data Coverage

TDS-1 can acquire a large quantity of dataset because of its on-board GPS processing capabilities allowing to have a global coverage of the Earth for a long period of time. This makes it possible to have various types of situations in terms of wind or wave height for the ocean reflections and type of surface reflected for land reflections. In this section, we will describe the coverage of the dataset used for the study.

3.3.1 Time period

The dataset contains data for a period of time going from September 2014 to April 2015. The table 3.2 gives the detail of the time and duration at which collection was taken.

| Collection | Date | Duration |
|------------|------------|-------------|
| RD000001 | 2014-09-01 | 52 min |
| RD000002 | 2014-09-01 | 20 min |
| RD000003 | 2014-10-06 | 8 min |
| RD000004 | 2014-10-14 | 8 min |
| RD000006 | 2014-10-30 | 14 h 46 min |
| RD000007 | 2014-11-08 | 9 h 3 min |
| RD000008 | 2014-11-15 | 47 h 38min |
| RD000009 | 2014-11-23 | 7 h 59 min |
| RD000016 | 2015-01-26 | 47 h 38 min |
| RD000017 | 2015-02-03 | 47 h 7 min |
| RD000018 | 2015-02-11 | 46 h 7 min |
| RD000019 | 2015-02-19 | 47 h 38 min |
| RD000020 | 2015-02-27 | 43 h 26 min |
| RD000022 | 2015-03-07 | 2 h 12 min |
| RD000023 | 2015-03-15 | 37 h 18 min |
| RD000024 | 2015-03-23 | 40 h 55 min |
| RD000025 | 2015-03-31 | 47 h 18 min |
| RD000026 | 2015-04-08 | 47 h 38 min |
| RD000027 | 2015-04-16 | 47h 38 min |

Table 3.2: Dates and duration of data by collection

The dataset although very large, does not cover continuously the eight months period. This can make the process of co-localisation² a difficult task as it will be presented later in this thesis.

3.3.2 Spatial coverage

The bistatic geometry makes it possible to obtain reflections indiscriminately from the position of the satellite. Indeed, contrarily to scatterometers or altimeters which emit the radio wave and are thus limited to their track, TDS-1 can potentially receive signals from any visible emitting GPS systems (4 simultaneous tracks are considered only).

The different collections have different coverage as they do not have the same duration. The figure 3.4 presents two examples of coverage by collection.

The collections which have a long time duration have obviously significantly more data available. Thus the collection RD000001 has only 32 tracks with a coverage of East Pacific when collection RD000006 has 252 tracks and a quasi global coverage.

As the reflections are not controlled, several types of land apart from water are sensed. This gives a significant amount of data which corresponds to ice, or soil bodies. The figure 3.5 gives the repartition of land types for a collection RD000009 which is representative of all the data available. The information is taken from the USGS Land Use/Land Cover³. *WaterBodies* is the prominent type of land available and it will be

² Process of finding geophysical data from different sources at the same time and place as the DDM

³ see https://lta.cr.usgs.gov/globdoc2_0

the main focus of the study. Data is then filtered accordingly to keep reflections over the ocean.

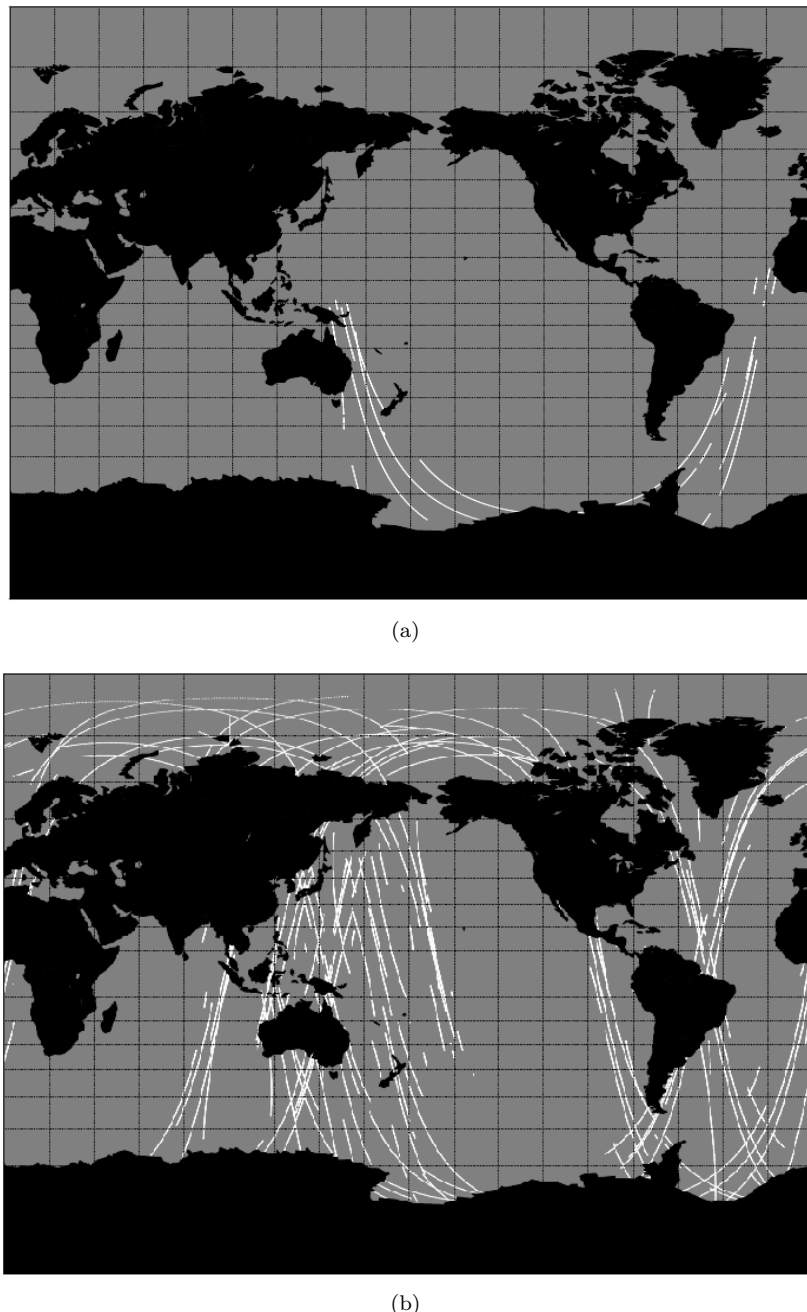


Figure 3.4: Coverage of collection RD000001 (a) and RD000006 (b)

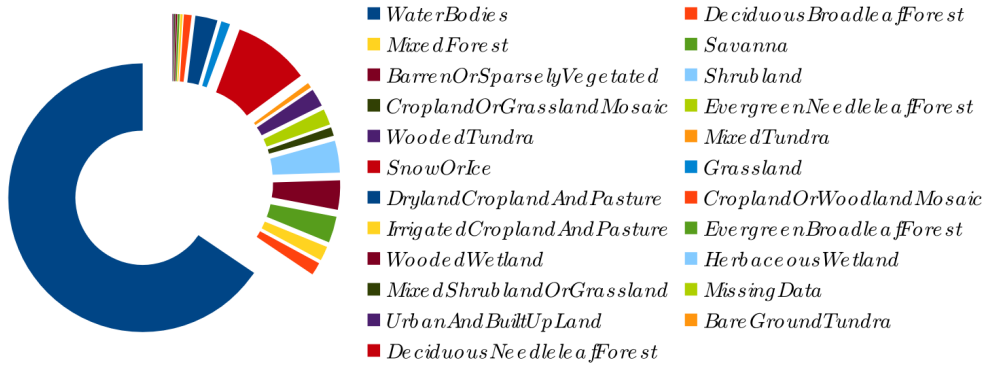


Figure 3.5: Example of repartition of land types

3.3.3 Storms co-localisation

The main objective of this study is the retrieval of wind through the data available. In this context, situations where a storm is under the scope of the satellite are interesting.

Indeed, these areas present great winds who are not common and it is interesting to see how the DDMs are impacted by such conditions. Moreover, these areas are mostly under rain cells which usually corrupt the radar signals with regular scatterometers. The GNSS-R signals are theoretically non impacted by these cells. The contribution of GNSS-R in this context is promising.

For these purpose, the SMOSSStorm+⁴ database is really useful. It contains information (localisation in time and space) about all the tropical storms known recently and provides wind data around the storm when available. The localisation is provided in form of tracks with latitude/longitude and time in UTC format. Each point of the track is separated from the next by 6 hours, which gives us a fairly good estimation of the trajectory of the storm.

This database was crossed with TDS-1 track metadata in order to find DDMs corresponding to storms events. The filters chosen are the following :

- The TDS-1 track pass within a 600 km range (corresponding roughly to the scope of the satellite given its altitude and an elevation from 90° to 45°).
- The time difference between the storm track and the TDS-1 track is less than 6 hours.

A single storm, named Nuri, corresponds to these criteria. The figure 3.6 presents 2 tracks of TDS-1 which are within the range of the storm (corresponding to the dot). The local wind speed field is provided as well by the ASCAT satellite.

The wind field over the surface is limited to $0 - 14 \text{ m.s}^{-1}$ which is not high if compared to the distribution of wind in non-storm areas. This makes this area not significant for a study. Using the SMOSSStorm+ database, we find that the storm is not yet formed.

⁴see <http://www.ifremer.fr/cersat/images/smosstorm2/>

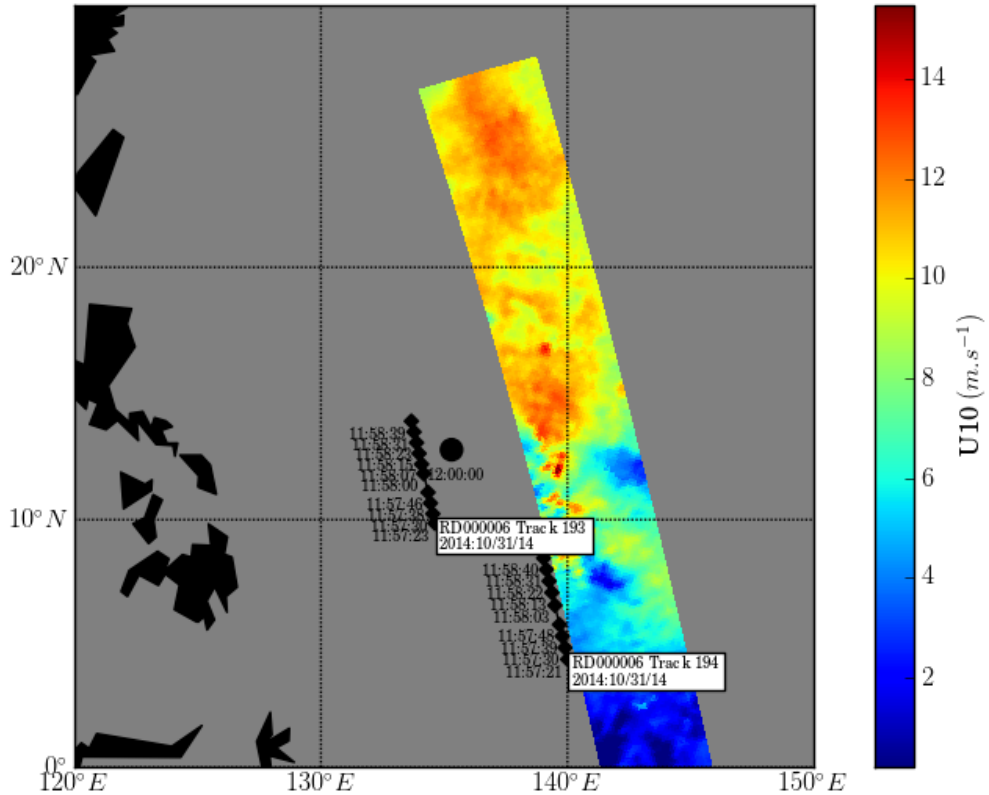


Figure 3.6: Flight over Nuri by TDS-1

The wind field will grow much stronger (about 40 m.s^{-1}) several days later.

The crossing of data with the SMOSStorm+ database reveals that no significant data from storms is available in our dataset. This was to be expected as storms typically occurs during the summer in the North's hemisphere which is not a period covered by TDS-1. We will then not focus our study on storms but rather explore the possibility to extract ocean surface winds from TDS-1 data.

Chapter 4

Implementation of a direct model using the Radar equation

This chapter describes an implementation of a model for the DDM resulted by the reflection of GNSS signals over the ocean's surface. It presents the parameters taken into account, the implementation and the results for several situations.

4.1 Coordinates system and Earth model

Coordinates Systems : The geometry of the problem is bistatic as presented in section 2.3. The same naming convention is used. The coordinates system is depicted in figure 2.4. The frame is centred at SPx (corresponding to the point of the surface with a minimum delay), the x-axis is on the surface's tangent plane and oriented towards Rx. This coordinates system will be called the "SP centred system".

The metadata files of TDS-1 give the localisation of the satellites and SPx in the ECEF coordinates system. The point (0,0,0) is defined as the center of mass of the Earth, the z-axis is pointing towards the north. The x-axis intersects the sphere of the earth at 0 latitude (the equator) and 0 longitude (Greenwich). For a comparison between the SP centred system and the ECEF see figure 4.1.

Earth Model : The shape of the Earth is an important parameter in the computation of distance between points over the ocean's surface. This shape is named the "Geoid" and it is the shape that the surface of the oceans would take under the influence of Earth's gravitation and rotation alone, in the absence of other influences such as winds and tides. It corresponds to the equipotential surface that would coincide with the mean ocean surface of Earth. Several approximations with different complexity are possible :

- The surface of the Earth's can be considered to be flat if the area considered has a dimension greatly inferior to the radius of the Earth.
- The approximation of the Earth as a sphere is widely used in various oceanographic applications.
- the WGS-84 (World Geodetic System) approximates the Geoid by an ellipsoid. It is used in most navigation systems.

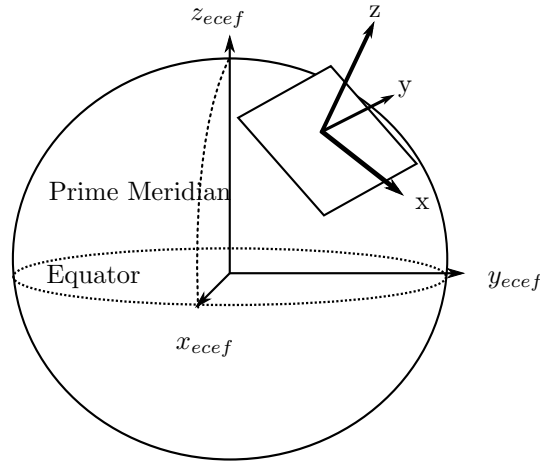


Figure 4.1: ECEF coordinates versus the SP centred system

The simulator takes into account these various models. It allows to see the impact of the Earth's curvature given our resolution of about 10 km.

4.2 Simulator specifications

The simulator, developed in Python, is a system that takes several inputs parameters for the computation of the waveform. The general organisation is presented in figure 4.2.

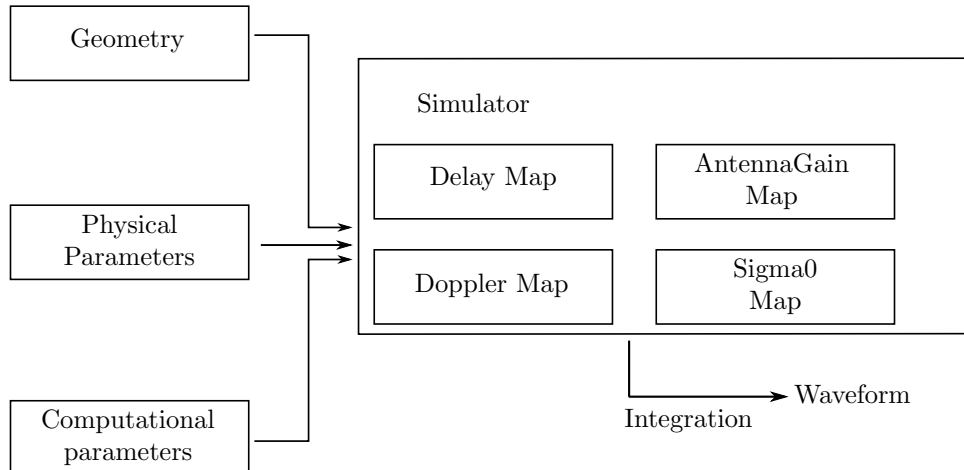


Figure 4.2: Organisation of the simulator

The simulator is decomposed in several steps. We first chose an area of the surface represented discrete points over the surface. The delay and Doppler associated for each point is then computed, resulting in Delay Doppler Map of the surface. The sea state is modelised by the repartition of σ_0 over the surface and the receiver antenna gain map over the surface is computed. Using these, the Radar Equation 2.5 is used to compute the power received.

The inputs of the system are the following :

- Computational parameters :
 - **dist** is the length of the side of the square of surface used for the computation.
 - **resolution** is the distance between two points on the grid and is used to control the density of points.
 - **Delay resolution** and **Doppler resolution** are the resolutions we want for the DDM.
 - **Doppler pixels** and **Delay pixels** are the number of the pixels we want to be processed for the DDM.
 - **Ti** is the integration time.
- Physical parameters :
 - **model** is the Earth's model chosen (flat, round or ellipsoid).
 - **lambda** is the wavelength of the signal.
 - **wind speed** is the wind over 10 m of the surface.
 - **wind dir** is the direction of wind in the frame described in the section.
- Geometry parameters :
 - **Rx**, **Rv** are the position and velocity of the receiver in ECEF.
 - **Tx**, **Tv** are the position and velocity of the transmitter in ECEF.
 - **SPx** is the position of the specular point (point at which the reflection is located considering the Geometrics physics approach) in ECEF.
 - **Attitude** is the orientation of the receiver satellite in the orbit's frame. It corresponds to three angles.

4.3 Computation of maps over the surface

As said in the section 4.2, the simulator computes several maps, which means to compute, for each point of the grid a value (Doppler shift, delay, σ_0).

σ_0 : the normalised cross section is computed using the KA-GO approximation which allows to write [Zavorotny et al., 2014]

$$\sigma_0 = \pi |R^2| \frac{q}{q_z} P(-q_x/q_z) \quad (4.1)$$

with :

- **q** = (**qx**, **qy**, **qz**) is the scattering vector defined as $\vec{q} = \frac{2\pi}{\lambda}(\vec{n} - \vec{m})$
- **R** is the Fresnel coefficient for the sea. At L band it is roughly 0.64.
- **P** is the repartition of the slopes as defined in section 2.2.

The repartition of σ_0 over the surface obtained is a Gaussian centred on SPx. We can find an example in figure 4.3, this map will model the sea state in the simulation.

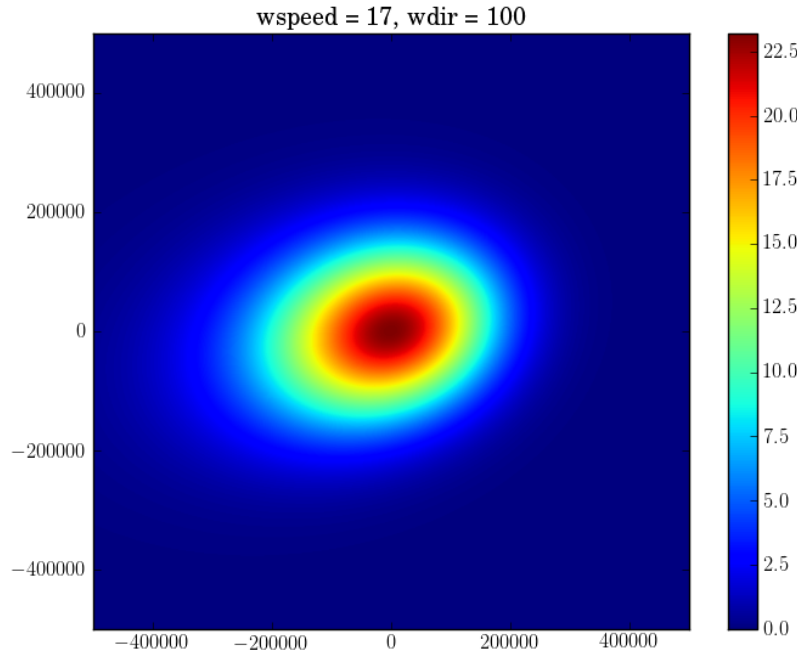


Figure 4.3: Example of σ_0 (dB) generated over the surface. Units are in meters.

Delay Doppler Map : Using the formulas presented in section 2.4.3, we can map the surface in term of Delay and Doppler shift. We can find an example of simulations in figure 4.4. The Delay and Doppler represented are normalised in order to make SPx the point at *delay* = 0s and *Doppler* = 0Hz. The model chosen here is important as the distances between the surface and the satellites is dependent of it.

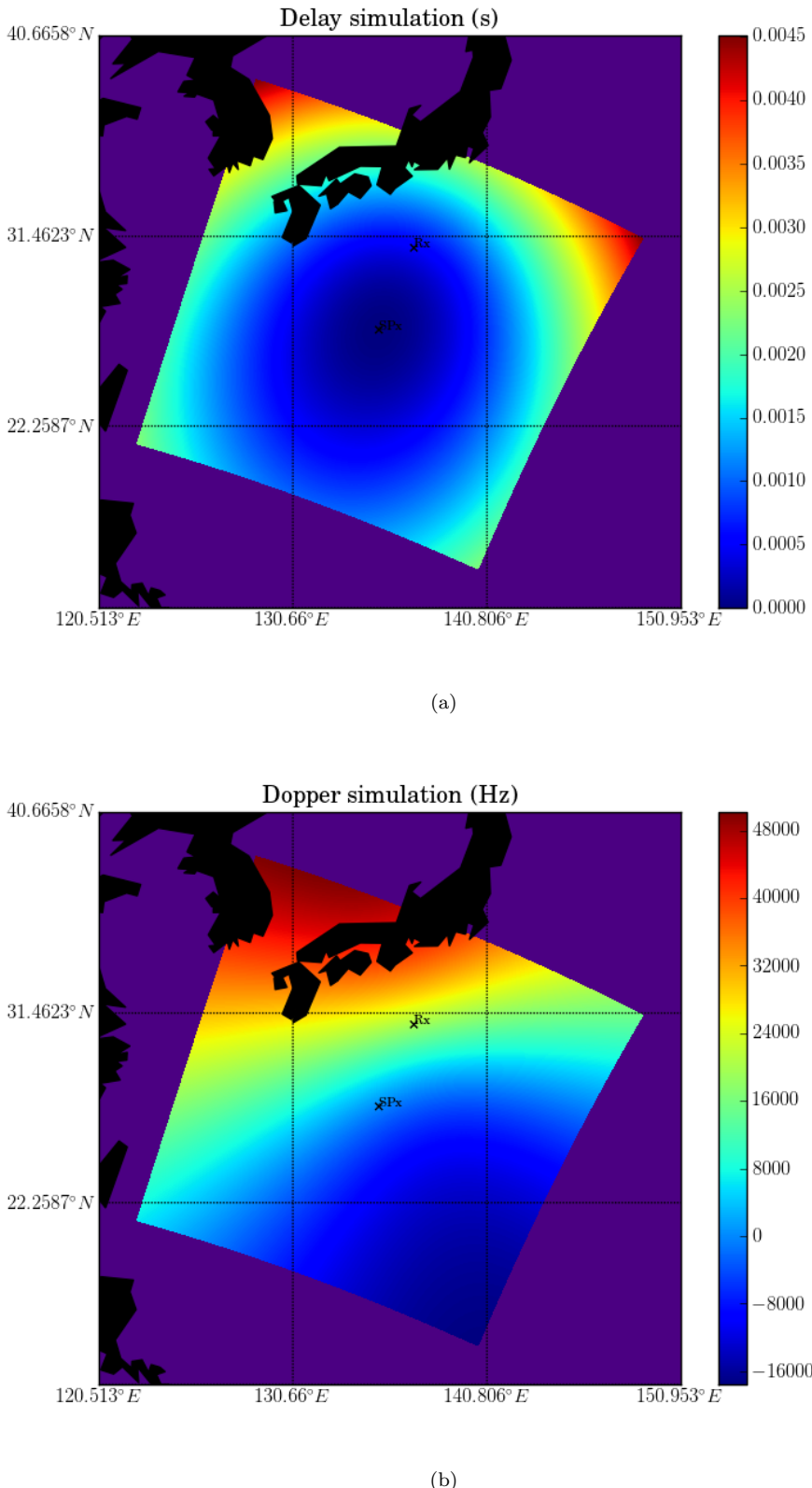


Figure 4.4: (a) Delay Map (b) Doppler Map for RD000003 track 11 at 2014-10-06T11:52:21.4567692

Antenna Gain Map : The antenna gain of TDS-1 is provided as an array of the gain in dB for discrete values of elevation and azimuth (angle of the rotation of the antenna around its axis). The elevation and azimuth is computed for each point of the surface and the gain is given by the corresponding value in the array. An example of map obtained is presented figure 4.5.

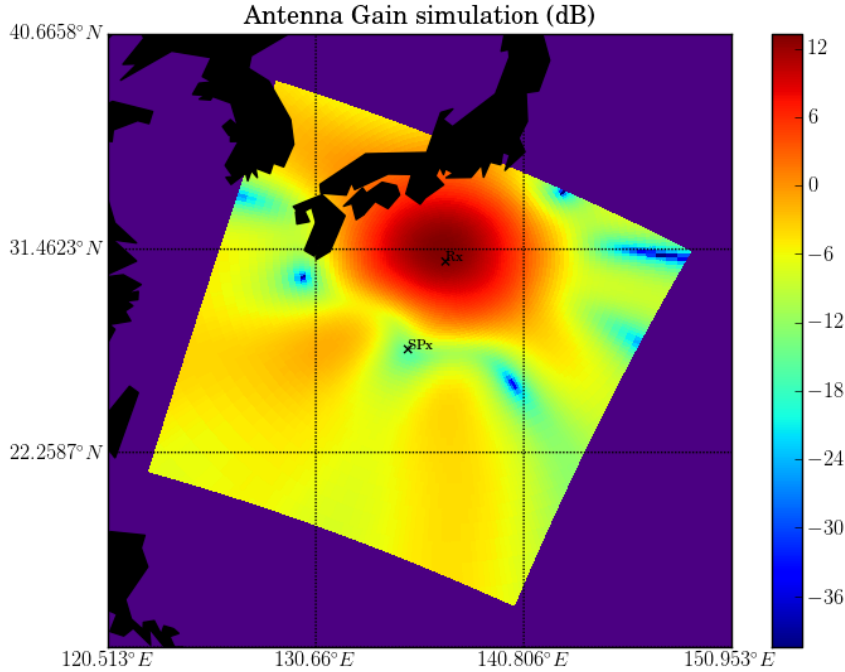


Figure 4.5: Antenna Gain (dB) for RD000003 track 11 at 2014-10-06T11:52:21.4567692

4.4 Results and Interpretation

This section presents the results of the simulation for several examples. For each example, the geometry is taken from a peculiar data from TDS-1. The table 4.1 gives the parameters common to all simulations if not said otherwise. The physical parameters are taken from TDS-1 specifications and the computational parameters are chosen as a compromise between the computation time and the resolution needed to compute accurate waveforms.

Waveform : The figure 4.6 presents a result of the simulation for the data RD000006 track 191 at 2014-10-31T12:00:13.9714486. The elevation is about 67° and the wind has a speed of $11m.s^{-1}$ and a direction of 119° in the SP centred frame. The plot gives the power for a Doppler shift of 0Hz (the DDM are centred so that the OHz corresponds to the Spx).

The power, given in dbW, does not represent the absolute power received at the receiver. Indeed, for the simulation, we do not have access to the power of the transmitter's antenna nor its antenna gain. They were thus not taken into account for the simulation.

| Parameter | Value |
|--------------------|-----------|
| lambda | 19 cm |
| Ti | 1 ms |
| model | Ellipsoid |
| dist | 450 km |
| resolution | 500 m |
| Delay resolution | 244 ns |
| Doppler resolution | 500 Hz |
| Doppler pixels | 20 |
| Delay pixels | 128 |

Table 4.1: Common parameters for Waveforms simulation

The start time is arbitrary chosen to be 10 times the Delay Resolution of the Waveform, which explains the peak location.

The resulting waveform has the shape expected from the section 2.4.4. The results of the Doppler spread are visible on the waveform and the characteristic variation of the power along the delay is obtained.

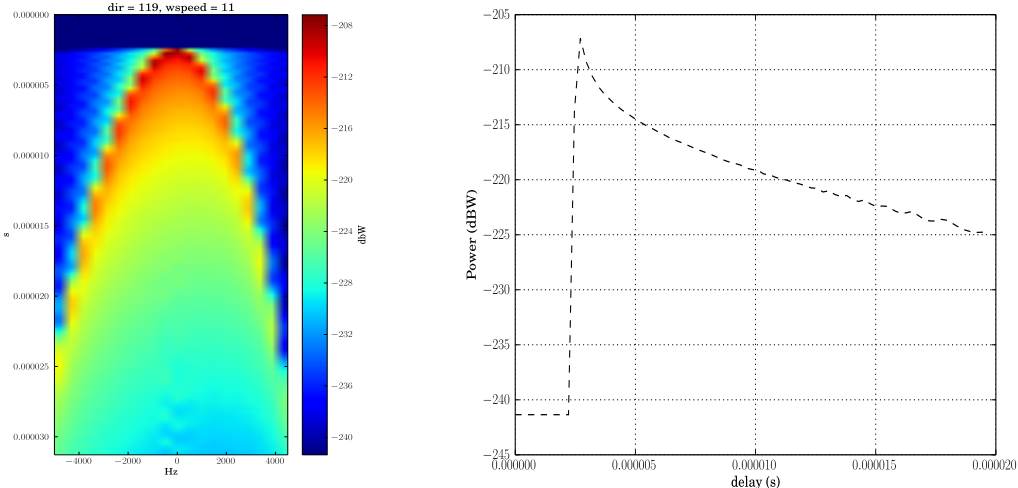


Figure 4.6: Simulated DMM and delay waveform for RD000006 track 191 at 2014-10-31T12:00:13.9714486

Comparison with Measured Waveforms : Several cases of TDS-1 DDMs were simulated in order to have a qualitative idea of the similarity between the simulated waveforms and the actual measured. The physical parameters for the simulation were taken from a co-localisation with the WW3 database which is presented in 5.2.

The waveforms are not aligned with the measured ones, which explains the difference of the peak location in delay. They were also normalised in order to contain the power in the interval [0 - 1].

- The figure 4.7 presents the case of a reflection at quasi-nadir, meaning an elevation angle near 90° and for a wind of $6m.s^{-1}$. The actual elevation is 87° .

The waveforms are similar in shape as the actual and simulated spreading are the

same. The simulated one is not as smooth as the measured one because of the limitation of the surface resolution in the computation.

It can be seen that the simulated one has a tendency to decrease faster in delay than the actual one. This could be explained by the fact that the sea state is not correctly described by the distribution of σ_0 . Moreover, the physical parameters in input are taken from WW3 which is a model and can under-estimate the local slopes.

- The figure 4.8 presents a case of a lower elevation angle.

It is interesting to see that again, the Doppler spreading are the same in the simulation and the measured DDMs. The spreading bandwidth was larger in 4.7, because the isoDelay ellipsoids were less sparse than here, resulting in isoDoppler zones attained earlier.

We can also notice that the waveforms are asymmetric. This is caused by the antenna gain which vary over the surface, causing the difference in power.

- The figure 4.9 presents the case of a specular reflection, meaning that the surface was smooth like a mirror.

In this case, the glistening zone is much shorter as no slopes will redirect the wave on the direction of the receiver.

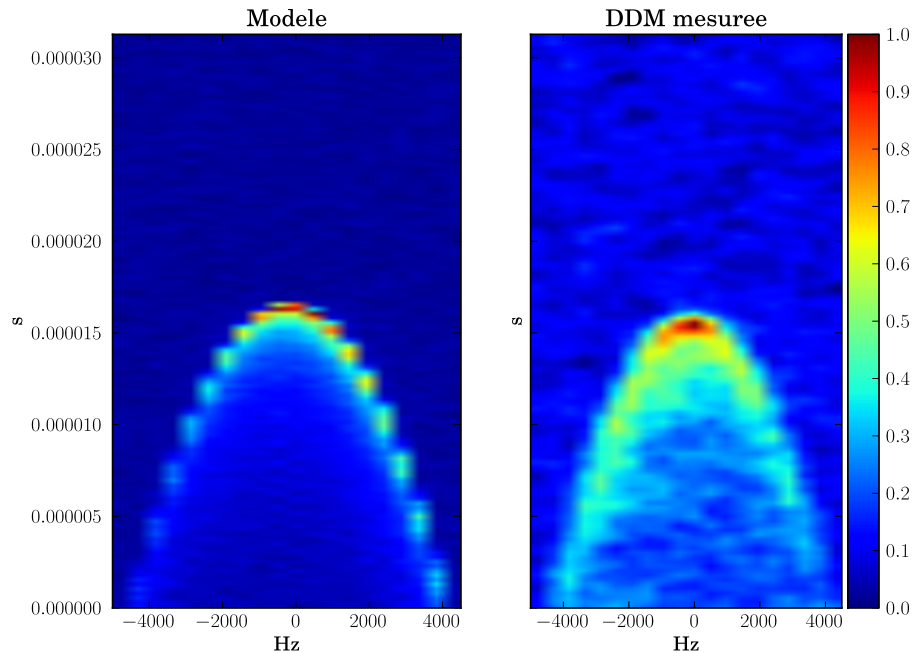


Figure 4.7: DDMs for RD000001 track 7 2014-09-01T10:48:19.4973256

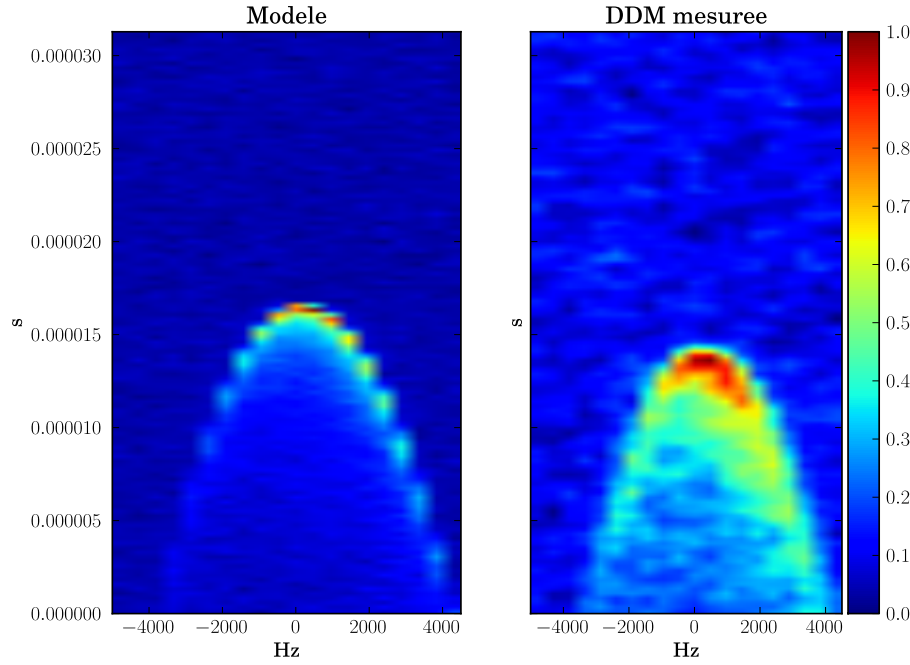


Figure 4.8: DMMs for RD000002 track 1 at 2014-09-01T20:11:05.8811101

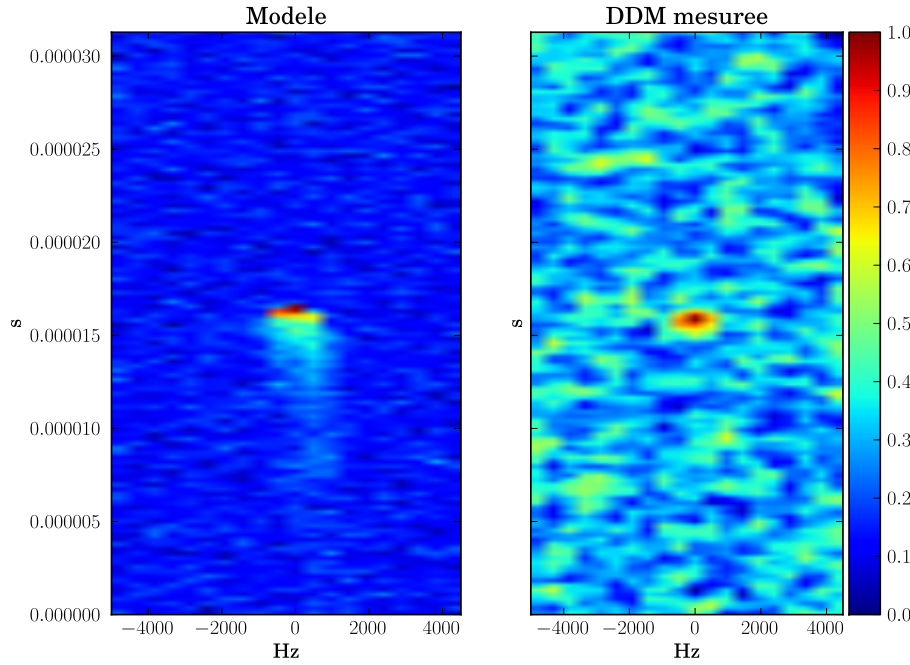


Figure 4.9: DMMs for RD000001 track 10 at 2014-09-01T10:56:16.4982748

Specular reflection : For a wind speed inferior to $2m.s^{-1}$, the reflection on the ocean's surface can be considered as strictly specular and the Doppler spreading effect is not seen. This is well shown in figure 4.10, where the same geometry as previously was chosen and wind speeds of $1.2m.s^{-1}$ and $1.2m.s^{-1}$. Several Doppler shifts are plotted

and no spreading effect is seen for the 1.2m.s^{-1} case when the 12m.s^{-1} case show that the power for the several Doppler-shifts is delayed.

The power has the form of a rapidly decreasing peak which is expected as the essential power scattered is done around the SPx.

The simulation tends to diverge when the wind speed is low as the local MSS is nearing 0 and the power received is inversely related to it. It can be noticed figure 4.11, that there is a limit at $w\text{speed} = 1\text{m.s}^{-1}$ between a rapidly divergent zone (specular) and a zone where the power is still limited. The simulation seems then not accurate for representing a specular reflection due to the Sea model chosen.

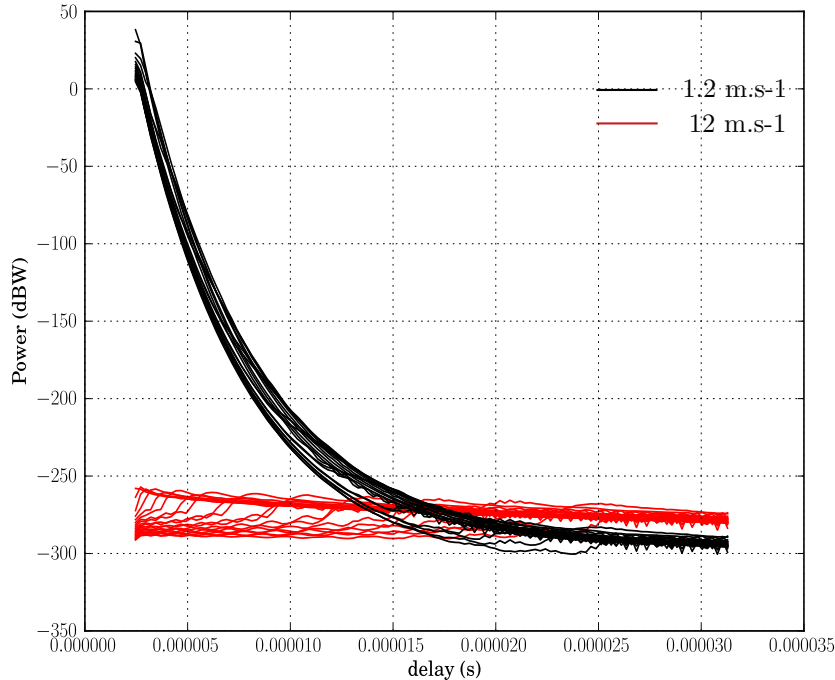


Figure 4.10: 1D waveform for the case of specular reflection vs non specular

Wind Speed : The figures 4.12 and 4.13 give the simulation of waveform for several wind speeds and a direction of 0° . The geometry is taken from RD000004 track 0 at 2014-10-14T21:48:11.9772487 and the elevation is about 88° (quasi-nadir). The sensitivity to wind speed is shown clearly in figure 4.13, where the peak varies with the wind speed. It can also be noticed that whereas the sensitivity is good for low wind speed, it has a tendency to saturate for greater winds. We can also notice that the slope of the decreasing part varies with the wind speed. These sensitivities will be useful when thinking of wind retrieval applications.

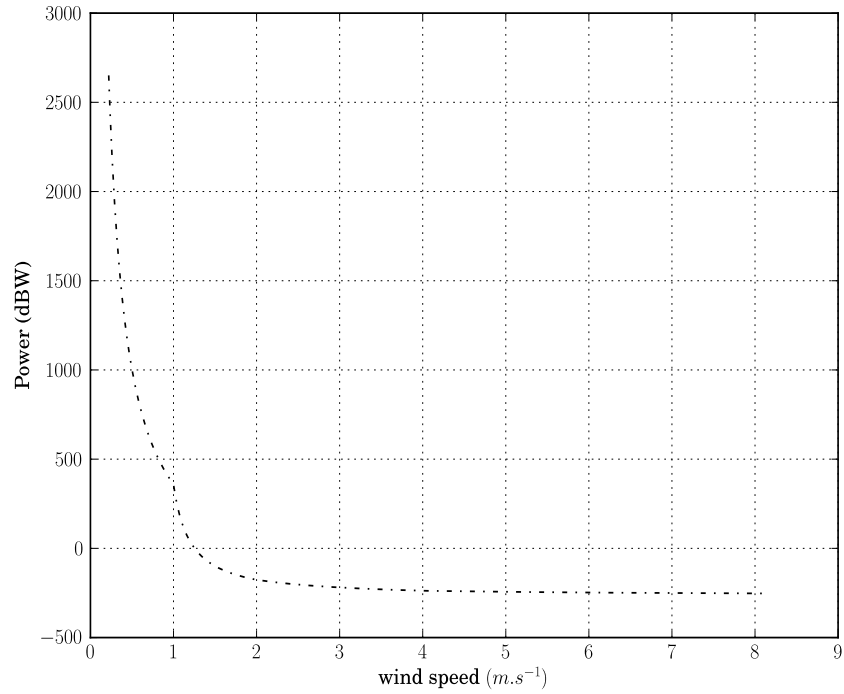


Figure 4.11: Power for several wind speed in a specular situation

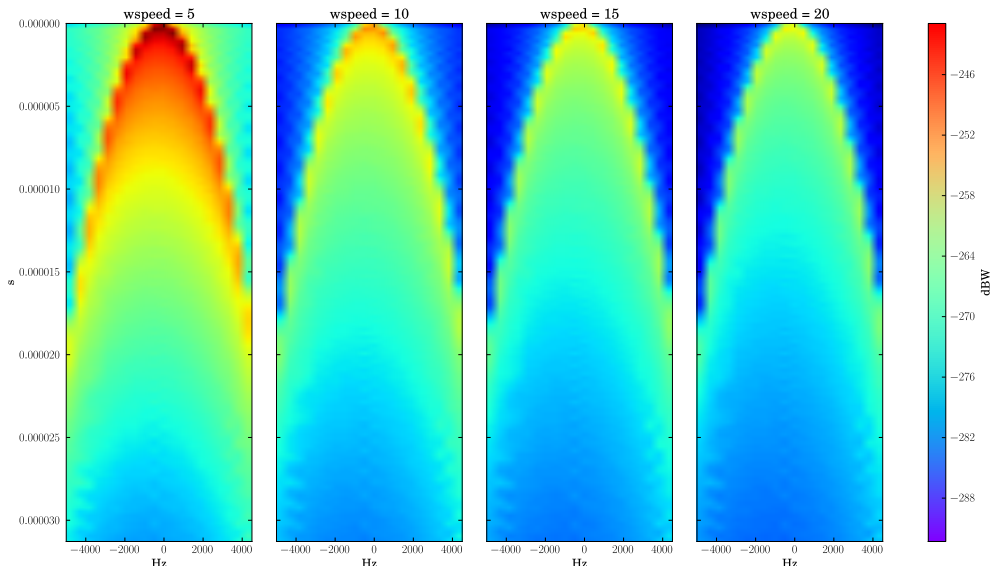


Figure 4.12: Waveform simulated for different winds speed for RD000004 track 0 at 2014-10-14T21:48:11.9772487

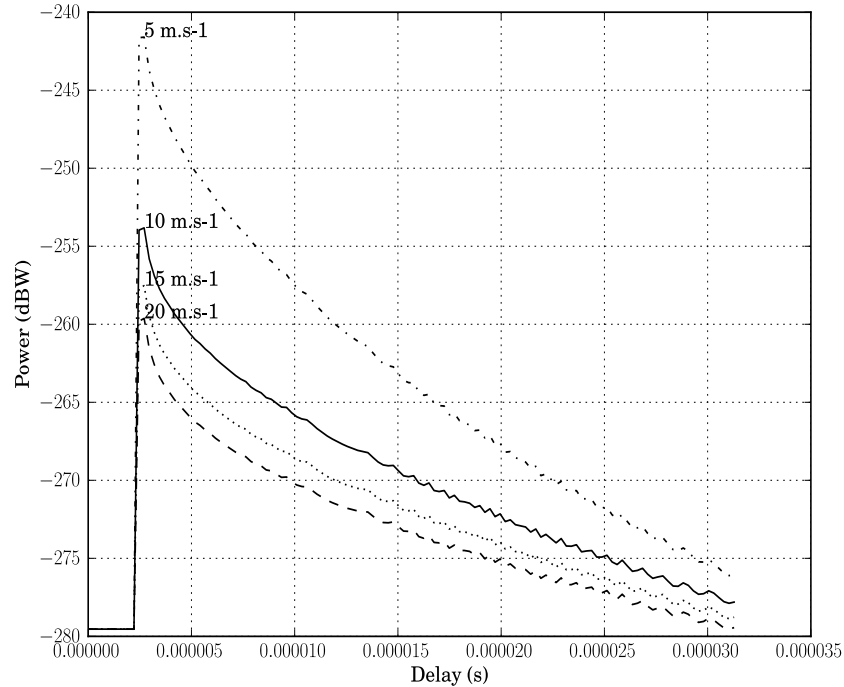


Figure 4.13: Waveform simulated (Doppler 0) for different winds speed for RD000004 track 0 at 2014-10-14T21:48:11.9772487

Wind direction : The figure 4.14 presents the waveforms simulated for several directions and a wind speed of $11m.s^{-1}$. The σ_0 map along with the isoDoppler are represented as well for each direction. It can then be seen that the wind direction can influence the power received for specific Doppler shifts. The σ_0 map show that the areas illuminated are dependant of the wind direction. These areas can be within the Doppler zones corresponding to the waveform or not, resulting in the difference between waveforms at $wdir = 80^\circ$ and $wdir = 0^\circ$ for example. The wind direction can then impact some parts of the waveform but we keep in mind that the power received at the SPx is the same for each direction.

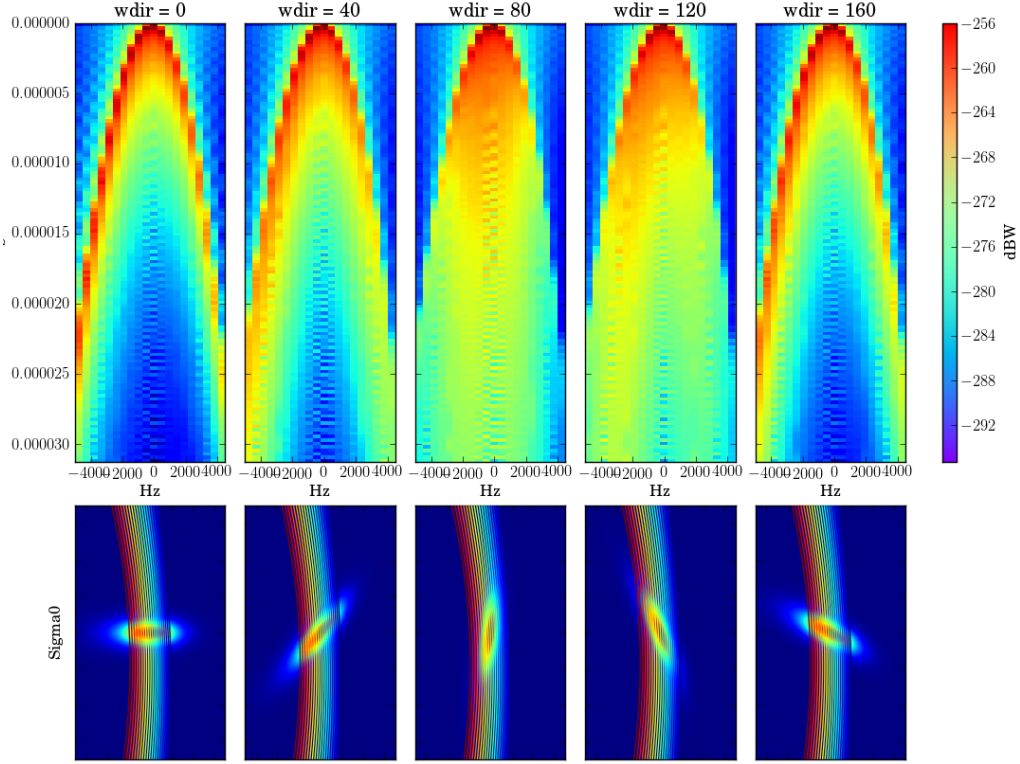


Figure 4.14: Waveform simulated for different winds speed for RD000006 track 191 at 2014-10-31T12:00:13.9714486

Elevation : The figure 4.15 is a plot of different waveforms simulated from different elevations angles taken from several points of the track 191 collection RD000006. The wind speed is fixed at $11m.s^{-1}$ and the direction is at 0° .

The waveforms are sensitive to the elevation. Indeed, the peak of power received varies with the elevation angle as shown in figure 4.15 (mainly due to the antenna gain). This sensitivity can be compared to actual Waveforms measured for the track in figure 4.16. It must be kept in mind that the waveform plotted are the result from reflections through different sea states contrary to the simulations. The waveforms are not exactly aligned, as the start time of the recording is not always separated from the beginning of the reflection by the same amount of time. We can nonetheless see the effect of the elevation on the power received. The waveforms at elevation below 60° are noisy which makes it impossible to assess the effect of the elevation at these points. The elevation angle is then an important parameter when taking into account the various parameters that impact the waveforms obtained.

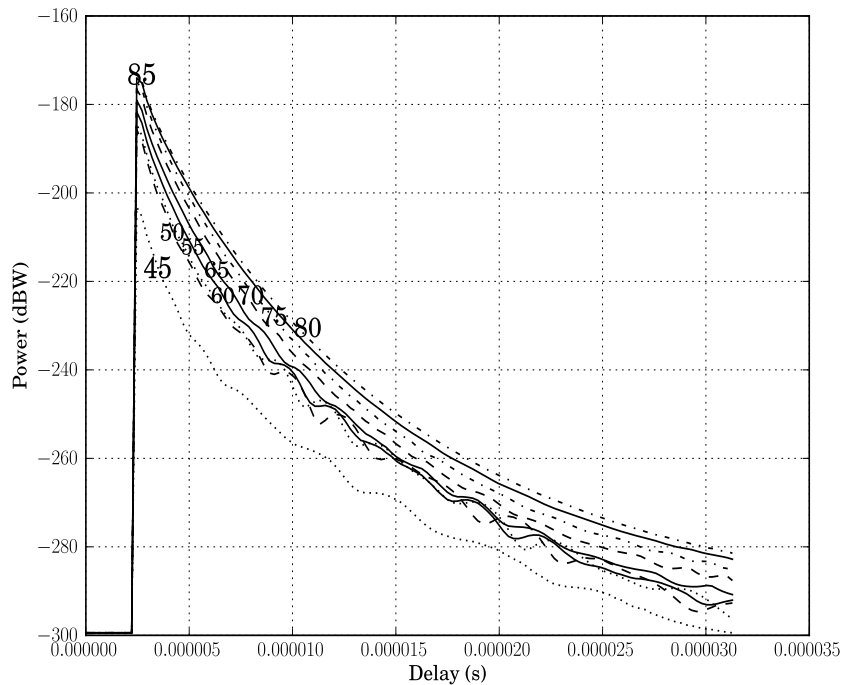


Figure 4.15: Waveform simulated (Doppler 0) for different elevations for RD000006 track 191

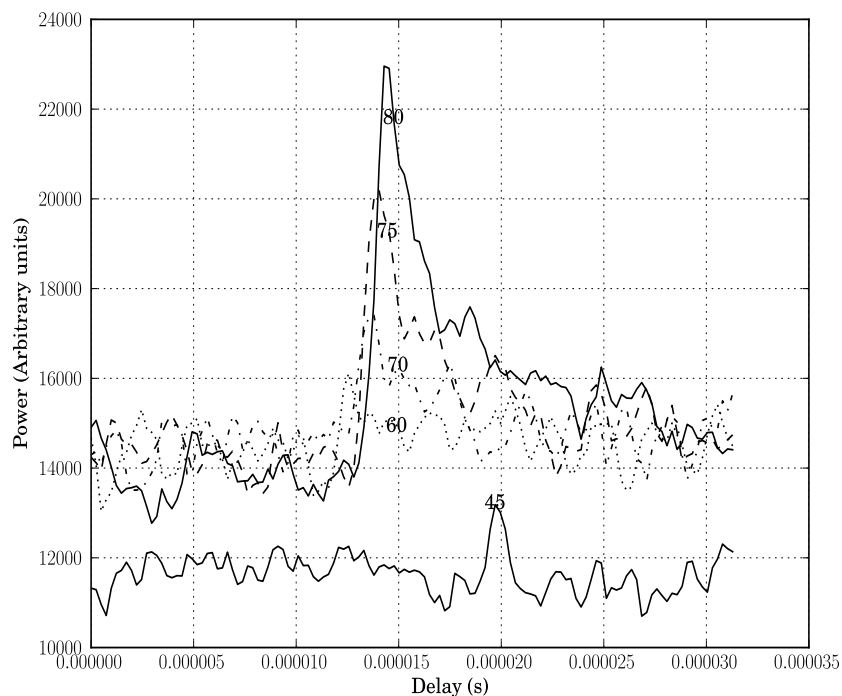


Figure 4.16: Waveform measured (Doppler 0) for different elevations for RD000006 track 191

4.5 Conclusion

We have implemented a model for the waveforms using the Radar Equation 2.5. The simulator takes into account several parameters to integrate numerically over a surface.

The simulator is interesting to assess the capabilities of wind retrieval through waveforms provided in TDS-1 dataset. It was demonstrated that it is not accurate for low wind speed as the power received diverges. Several simulations have shown that the waveform power peak is dependent of parameters such as wind speed or elevation.

The simulator has shown a sensitivity of the to wind speed through the peak of the power received, which is interesting for the next chapter.

Chapter 5

Inversion of TechDemoSat-1 Waveforms

The previous chapter has shown, through an implementation of a model, that the waveform obtained through the GNSS-R technique has a sensitivity to wind speed. This chapter aims at presenting methods developed in order to recover information about wind speed using TDS-1 data.

5.1 General principle

There are two approaches when trying to invert waveforms to retrieve geophysical parameters. The first consists in the fitting a theoretical model and the latter is based on an empirical approach.

We can find in [Gleason, 2006] or [Zavorotny et al., 2014] a thorough description of the means available in both approaches. The principles are the following :

- The theoretical approach use a direct model as developed in chapter 4 to generate several waveforms using different geophysical parameters. A cost function computing the dissimilarity between the waveform measured and the ones simulated is computed and the one with the minimum distance is chosen to give the geophysical parameters. The CYGNSS baseline algorithms will be mainly based on this approach.
- The empirical approach is based on DDM metrics. It chooses relevant parameters of the DDM as a representative and compare them to geophysical parameters (used as Ground Truth) coming from other sources. The aim is to develop a GMF (Geophysical Model Function) which is a transfer function between the waveforms and the wind speed. It is achieved through regressions.

In our case, the first approach is not feasible. Indeed, the SGR-ReSI is calibrated in an automatic gain mode which means that the Power of the waveforms is not absolute. Between two different waveforms, the same level does not correspond to same power received at the Antenna. It is used in order to dynamically collect waveforms from various geometries and keep a good signal to noise ratio. Unfortunately, the information about the gain for each waveform is not provided so it cannot be compensated resulting in the inability to use the theoretical approach.

The second approach was then used to estimate the wind speed.

5.2 Co-localisation with WW3 and ASCAT

One of the first step in the inversion of waveforms is to have a reference of wind speed, for the purpose of doing regressions or for assessing the result of the processing. This section presents the co-localisation of TDS-1 dataset with two databases : the WW3 and ASCAT.

WW3 Model and ASCAT mission :

- The WW3 (Wave Watch 3¹) is a based on a model developed by the NOAA. It provides global maps of the wind speed, wind direction and significant wave height.
- The ASCAT (Advanced SCATterometer) is one of the instruments carried on-board the Metop (Meteorological Operational) polar satellites launched by the European Space Agency. It is a real aperture radar that uses back-scattered waves to estimate parameters such as wind speed or wind direction.

Both datasets were provided by the Ifremer as arrays indexed by time, longitude and latitude. The table 5.1 gives the characteristics of the datasets. An example of Global map provided by WW3 is presented as well in figure 5.1.

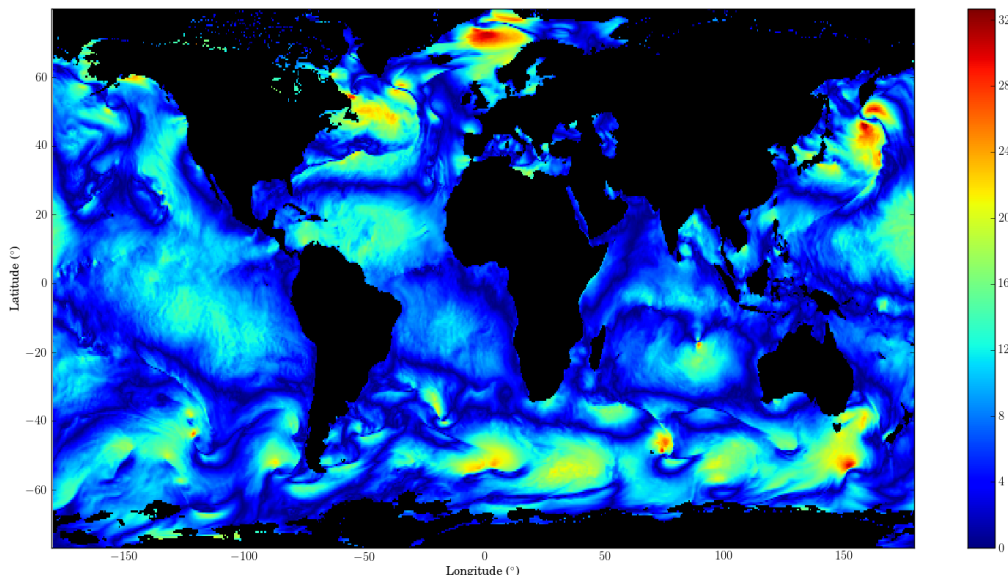


Figure 5.1: Example of global U10 ($m.s^{-1}$) map provided by WW3 at 30/12/2012 12:00:00

Comparison between ASCAT and WW3 : As presented in table 5.1, the two databases present different resolutions and comes from different sources. Whereas WW3 is a model and has a time resolution of 3 hours, ASCAT comes from a direct measurement but the gridded product has a time resolution of 24 hours. The swath product has not been considered in this study. The spatial resolution is better for ASCAT as well.

The problem with ASCAT database is the time resolution which is too low. Indeed, the wind speed has the time to change in the time lapse of a day. Thus, the map provided

¹see <http://polar.ncep.noaa.gov/waves/index2.shtml>

| | WW3 | ASCAT |
|----------------------|---------|----------|
| Type | Model | Measured |
| Time resolution | 3 hours | 24 hours |
| Longitude resolution | 0.5° | 0.25° |
| Latitude resolution | 0.5° | 0.25° |

Table 5.1: ASCAT vs WW3

are averages of the wind speed at a given location for a day. WW3 has not this problem as the time resolution is of 3 hours which is more interesting for our purpose of wind retrieval.

The figure 5.2, gives an histogram of the repartition of wind WW3/ASCAT for a time period of several months. It can be seen that, most of the time, both winds are coherent. Variations can be accounted by the differences in resolutions between ASCAT and WW3, and by the fact that WW3 is a model.

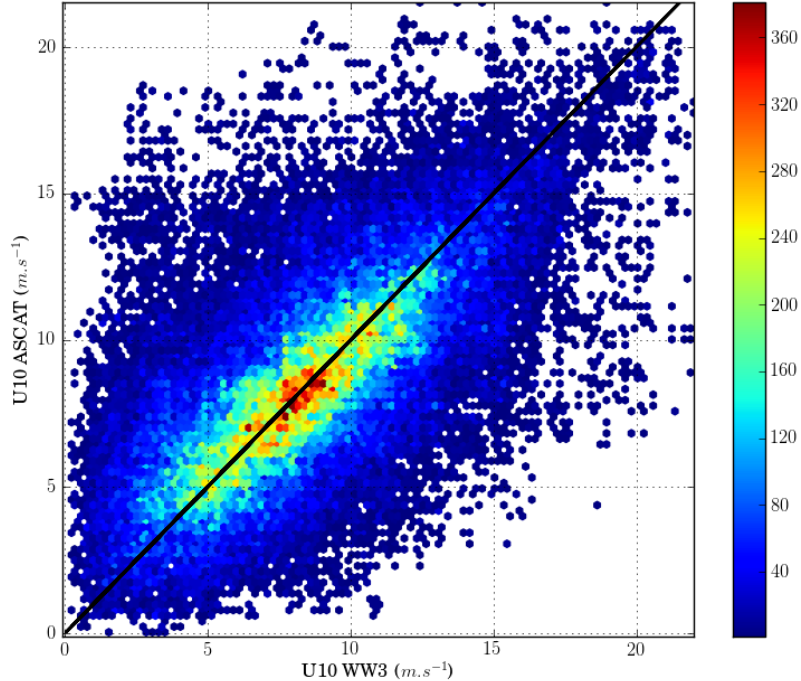


Figure 5.2: Histogram of ASCAT and WW3 wind

Given the histogram, it was chosen to use only WW3 for the purpose of doing regressions. Indeed, the time resolution is better and the wind is coherent with ASCAT which makes it better suited.

As the resolution is limited, the strategy for co-locating data is to find, for each waveform, the nearest point in time and space between the position of SPx and the

WW3 grid.

5.3 Selection of TechDemoSat-1 Data

The next step is to filter the TDS-1 dataset in order to keep only the high-quality waveforms. Indeed, we saw in section 4.4 that some waveforms are not usable as they are too noisy. This section presents the filters used and the parameters of the waveforms kept in order to do the inversion.

5.3.1 Filters on Data

In order to keep usable data, the following filters were used to select data :

- **LandType** : data corresponding to the flag *WaterBodies* is kept in order to have waveforms originating from ocean reflection.
- **AntennaGainTowardsSpecularPoint** : waveforms for which the Antenna Gain is inferior to $0dB$ at the Specular Point are filtered in order to limit the noise.
- **U10** : waveforms for which the co-localisation with WW3 gave a wind speed inferior to $1m.s^{-1}$ are filtered to avoid specular reflections.
- **hs** : waveforms for which the co-localisation with WW3 gave a hs inferior to $1m$ are filtered to avoid specular reflections.

These filters are approximately the same as the ones used in [Foti et al., 2015].

5.3.2 SNR as parameter from the waveform

We saw in section 4.4 that the waveforms' peak Power is sensitive to the wind speed and the elevation. This value is then interesting in the process of inverting the waveform to retrieve the wind speed.

As said in section 5.1, the SGR-ReSI is in automatic gain mode which makes absolute Power measurements not relevant. To resolve this problem, we use the SNR as the parameter of the waveform. Indeed, the noise is not dependent on the geometry but rather on the instrument and the type of surface illuminated. We can then consider that it is approximately the same for each waveform. The SNR can then be used as a parameter to represent the relative Peak power between the waveforms.

SNR Computation: If we compute the SNR as in equation 5.1, we can have a relative comparison between the Peak of the waveforms. The figure 5.3.2 illustrates the computation of the SNR. $\langle S_{peak} \rangle$ is computed as a mean of the neighbouring pixels of the Peak and $\langle N \rangle$ is a mean of the pixels just before the peak (representing the noise level). This method was used in order to compute the SNR in [Foti et al., 2015] as well.

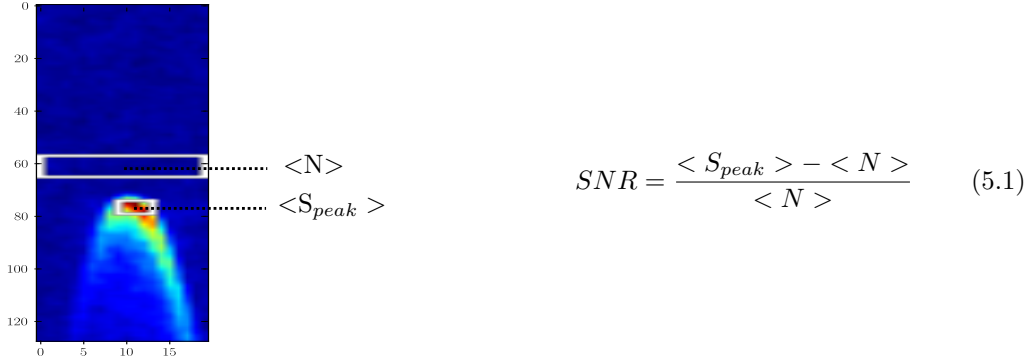


Figure 5.3.2: Computation of SNR

Peak detection : To compute the SNR, we first need to locate the position of the Peak in the Waveform. This can be achieved by means of Image Processing. Indeed, the peak location can be viewed as a contour detection. Thus an algorithm based on filtering by a Gaussian kernel and finding the maximum of the 2D gradient of the image was developed. The Gaussian filter allows to filter the noise in order to detect more easily the position of the maximum of gradient. The figure 5.3 gives an example of computation of the gradient after filtering and the location of the peak detected as well of the area used for compute the Noise power.

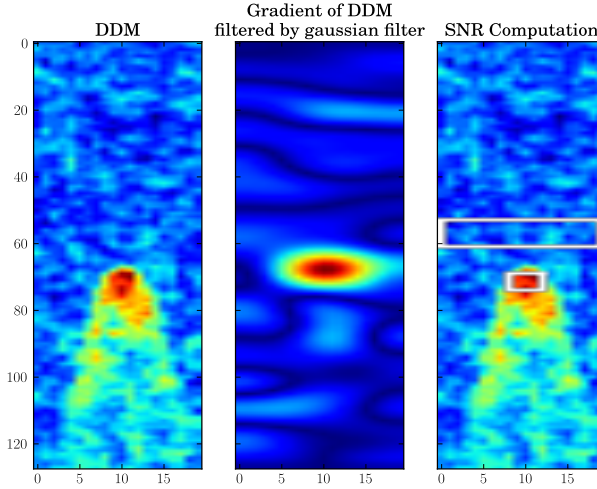


Figure 5.3: Example of computation of SNR

Choice of the size of Gaussian kernel : The choice was made in order to minimize the probability of error. To this end, 140 waveforms were selected from TDS-1 database (High-quality to noisy) for which the peaks were located manually. Then the distance between the detected pixel and the true one is computed.

Two thresholds were decided at a distance of 3 pixels and 9 pixels. As the neighbourhood used to compute the mean of SNR is 4×4 below the Peak pixel, these distances guarantee that it is within the neighbourhood. The result presented in figure 5.4, give a minimum of a size 4×4 for an error of 9 pixels. It was then chosen for the detection of the peak

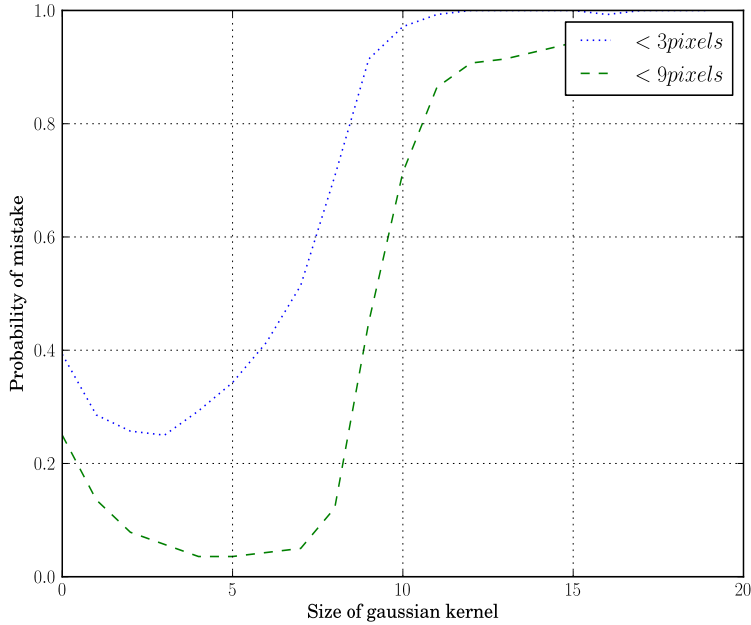


Figure 5.4: Probability of mistake for different sizes of Gaussian Kernel

5.4 First results of co-localisation

According to the section 5.3, the dataset was filtered and for each waveform remaining the SNR was computed. The wind speed was also taken from WW3. There is **767594 points** remaining at this point. The first results are presented here.

SNR as a function of U10 : The figure 5.5 presents the plot of the SNR computed in dB versus the U10 obtained from WW3.

The plot presents some disparity : some points seems to follow this tendency and are packed and others, less numerous, seems to be random. Thus, the dataset was cleaned from these points. The points that are within 3 times the standard deviation were kept and the others were deleted. The remain dataset accounts for **695141 points**, and is plotted in figure 5.6.

A global tendency of the SNR to decrease as U10 grows is observed, which is expected according to the model developed in chapter 4. The variance is nonetheless high ($\simeq 14$) which means that for a given U10, it is difficult to find a unique SNR corresponding. A GMF of the form $\text{SNR}(\text{U10})$ is not possible given this fact.

It can also be noticed that the sensitivity is lower for high winds ($U10 > 10m.s^{-1}$) and the SNR tends to saturate. This means that for a given SNRdB, several winds correspond as well, which is a problem of the retrieval of high winds.

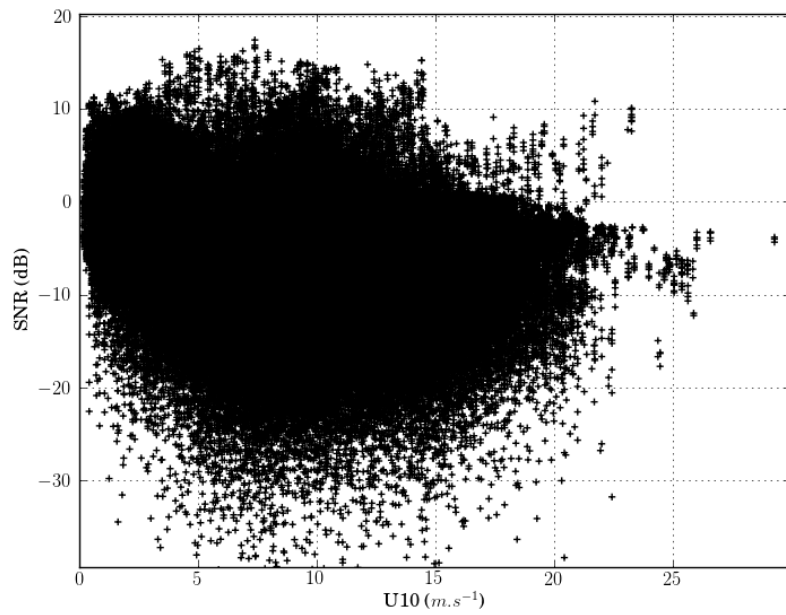


Figure 5.5: SNR(U10)

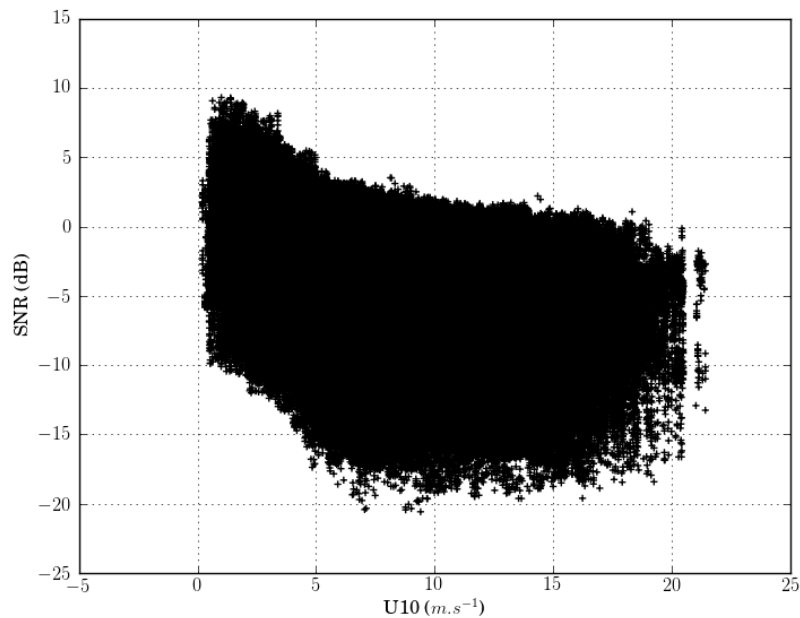


Figure 5.6: SNR(U10) after cleaning

SNR as a function of U10 and elevation : The figure 5.7 presents the same plot as figure 5.6 but with the elevation as the colour of the points. The figure 5.8 presents a mean of the plot by range of elevation of 5° .

The plots shows clearly the sensitivity of the SNR in terms of elevation angle which is an interesting result. Indeed, it allows to reduce the variance of the dataset as we can class the points by their elevation. We can then imagine a GMF in the form of $\text{SNR}(\text{U10}, e)$.

The problem of the saturation is well shown in figure 5.8, where the plots saturate at higher wind.

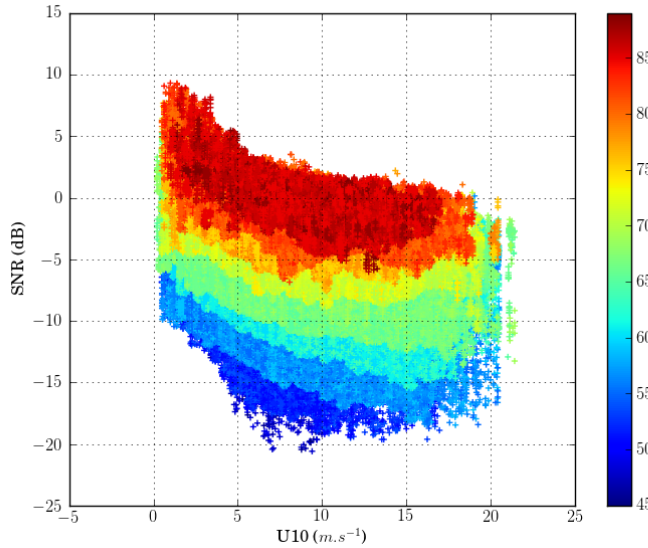


Figure 5.7: $\text{SNR}(\text{U10}, e)$

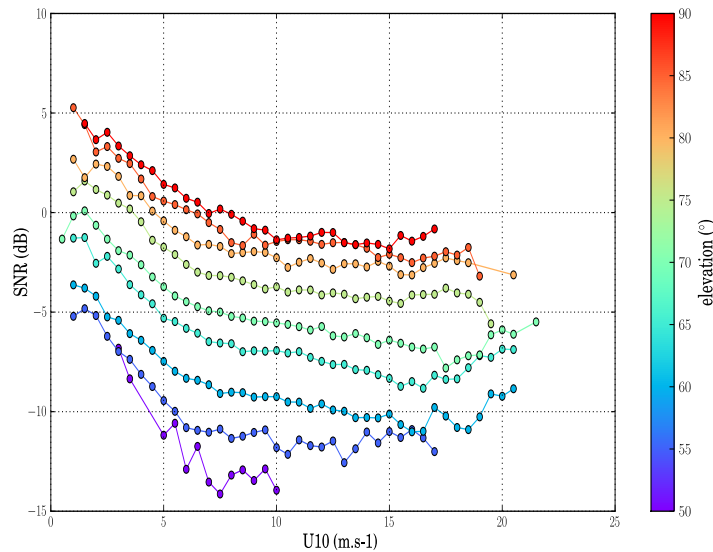


Figure 5.8: Mean $\text{SNR}(\text{U10}, e)$

5.5 Regression using a model and least squares minimisation

5.5.1 Model and Optimisation problem

In order to find a GMF, an optimisation approach is used. We use a model function F with several parameters unknown and which will be determined by the means of an optimisation problem. The method used is the least squares optimisation.

Principle : Be the model function $F(X, p)$, with the set of parameters $P = (p_1 \dots p_n)$ of size $1 \times p$ (p parameters), the dataset $X = (x_1 \dots x_n)$ of size $N \times M$ (N variables and M points), and a target $Y = (y_1 \dots y_n)$ of size $1 \times M$. We define the cost function :

$$J(X, Y, p) = \sum_{i=1}^M \|F(x_i, p) - y_i\|^2 \quad (5.2)$$

The problem is then to find the parameters which minimise the cost function. This allows us to have a GMF tailored to be as close as possible to the observations.

Model Functions : Given the results of the section 5.4, we can think that we have to take into account the SNR and the elevation in the GMF. We add to this the Antenna gain at the Specular Point.

From the variations of the SNR(U10) plot, it can be intuited that an exponential or a logarithm function is suited for a model function. Two model functions were then put into place :

- $F_{exp} = a * exp[b * log(\frac{K*SNR_{dB}}{\sin(e)} + K_1 * Ag_{dB} + K_2)] + L$
 $p_{exp} = (a, b, K, K_1, K_2, L)$
- $F_{log} = a * log(\frac{K*SNR_{dB}}{\sin(e)} + K_1 * Ag_{dB} + K_2) + b$
 $p_{log} = (a, b, K, K_1, K_2)$

Algorithm used : The minimisation is done numerically as the problem has a great number of parameters and the dataset is consequent. The algorithm used for this purpose is the Non-Linear Bound-Constrained Levenberg-Marquardt method. A description of this algorithm can be found in [Shan, 2006].

This algorithm is used primarily for its possibility to put bounds on the parameters during the minimisation which is necessary in our context. Indeed, given the model functions, we can't have the expression $\frac{K*SNR_{dB}}{\sin(e)} + K_1 * Ag_{dB} + K_2 \leq 0$. Otherwise, the result cannot be computed and the minimisation cannot continue as it uses the precedent results at each iteration.

The library SciPy of Python and more particularly the lmfit² wrapper around it, implements this algorithm and gives an elegant way to put constraints on the optimisation. This library was very useful in our problem of curve fitting.

²see <https://lmfit.github.io/lmfit-py/>

5.5.2 First results and performance

For the purpose of doing regressions, data was put into groups of elevation in order to evaluate the performances given a certain range of elevation. This was done because the elevation is a good measurement of the quality of the DDM, so low elevation means noisy DDMs and the regression will take it more into account. Thus, in theory, the results shall be better with higher elevations. The table 5.2 gives the ranges chosen and the number of points corresponding.

| Range Elevation | Number Of Points |
|-----------------|------------------|
| 60 - 90 | 453773 |
| 70 - 90 | 350459 |
| 80 - 90 | 74049 |

Table 5.2: Number of points by range of elevation

The dataset is separated in a training set for doing the regression and a test set for computing the performance of our regression. For a given set, 80% of the points were put into the training set and 20% in the test set.

The results of the regression are presented in the tables 5.3 and 5.4. The results of the inversion on the test set for the logarithm model are presented in figures 5.9, 5.10 and 5.11. The colour represents the number of point in the bin considered.

| a | b | K | K1 | K2 | L | Bias | Variance |
|---------|--------|---------|--------|---------|---------|---------|----------|
| -16.986 | 0.6147 | -0.6471 | 764.01 | 0.8664 | 1021.6 | -0.0068 | 10.172 |
| 198.56 | 0.0769 | 15.302 | 689.19 | -20.325 | -315.32 | 0.0023 | 8.8269 |
| 953.66 | 0.0161 | 47.658 | 1534.0 | -84.098 | -1063.9 | 0.0097 | 8.2785 |

Table 5.3: Results of Regression with exponential model

| a | b | K | K1 | K2 | Bias | Variance |
|--------|---------|---------|--------|---------|---------|----------|
| 0.4688 | 6.5254 | -5.5894 | 142.10 | -2.3679 | 0.0284 | 13.728 |
| 25.265 | -112.07 | 3.0857 | 141.21 | -4.1042 | 0.0054 | 8.7788 |
| 18.342 | -80.313 | 3.9007 | 136.05 | -7.0490 | -0.0100 | 8.4262 |

Table 5.4: Results of Regression with logarithm model

The results show that both model are more or less equivalent, except for the range 60 - 90, where the regression on logarithm model does not have any wind dynamic (see fig 5.9). Both models allows an estimator with a low bias which is a good point. The variance is not as goodThe variance is better for higher range of elevations which was expected.

The figures 5.10 and 5.11 show that the wind obtained saturates after $15 m.s^{-1}$. This can be explained by the fact that the SNR saturates at this point too. This can also be explained by the histogram of the wind used for the regression (see 5.12). Most of the wind available is in the range $5 - 10 m.s^{-1}$, so during the process of minimising the least squares their contribution is greater than for high winds.

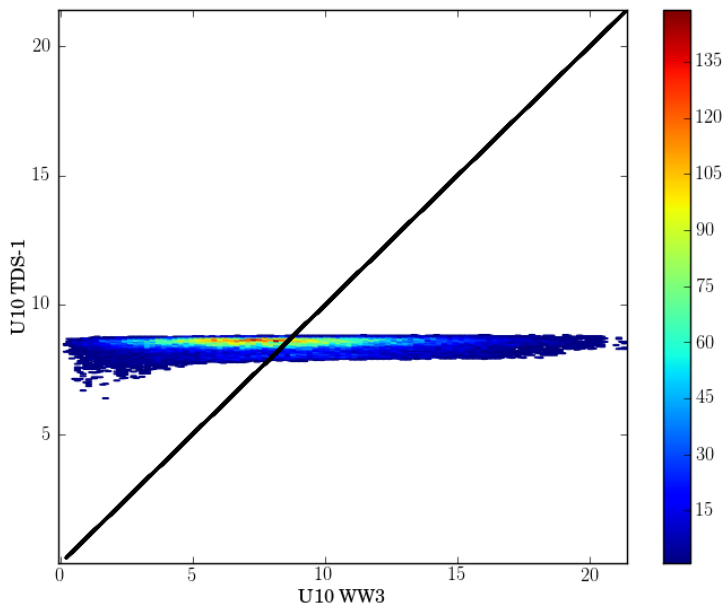


Figure 5.9: Results of the regression on the test set for range 60 - 90

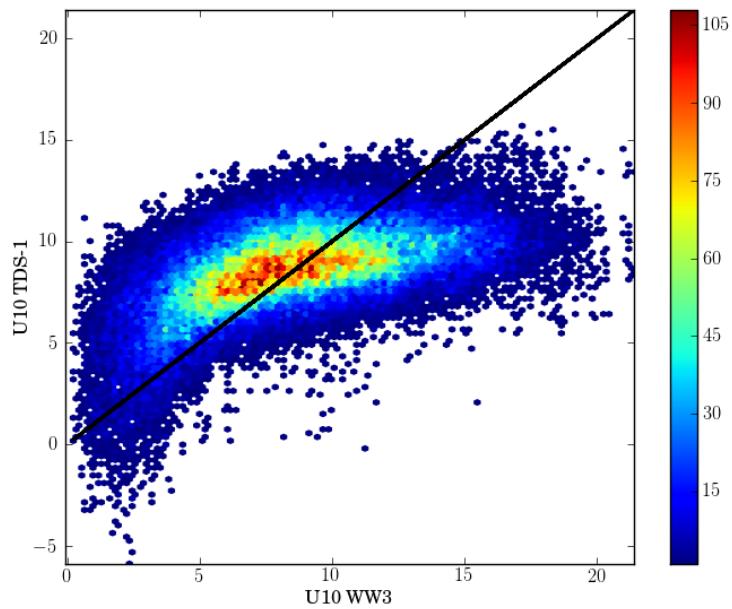


Figure 5.10: Results of the regression on the test set for range 70 - 90

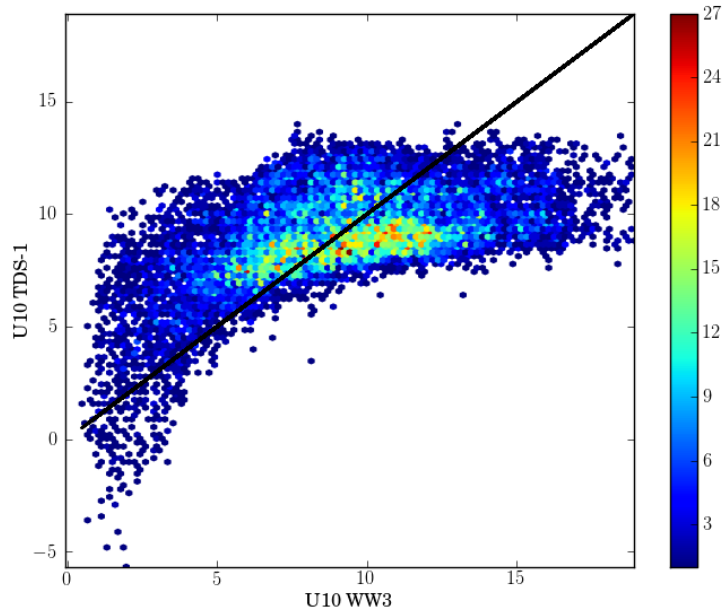


Figure 5.11: Results of the regression on the test set for range 80 - 90

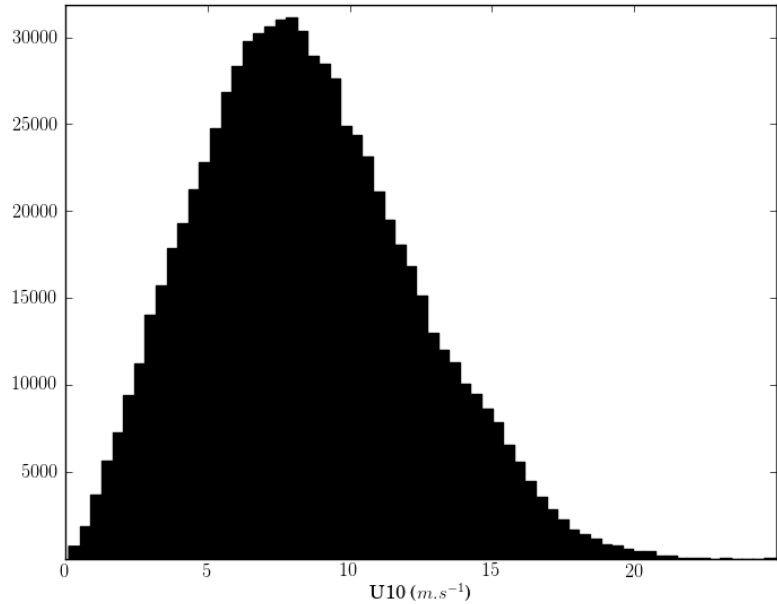


Figure 5.12: Histogram of the wind Ww3

The regression show interesting results for the range of wind $0 - 15 \text{ m.s}^{-1}$ but is not accurate any more for higher winds. The bias and the variance for the interval [0 - 15]

| Range | Bias | Variance |
|---------------|-----------|----------|
| $<15m.s^{-1}$ | 0.341427 | 6.532214 |
| $>15m.s^{-1}$ | -5.759717 | 2.264347 |

Table 5.5: Bias and variance by range of wind

and [15, 30], for the case in figure 5.11 are presented in the table 5.5. The estimator become biased for great winds which is problematic.

To accurately obtain these winds, conditions have to be added to the problem. These will be discussed in the next sub-section.

5.5.3 Weighted regression

In order to obtain a GMF accurate for high winds, the contribution of the lower winds in the regression can be lowered. To this purpose, we associate a weight w_i to each point of the training set and minimise the new cost function :

$$J(X, Y, p) = \sum_{i=1}^M w_i \times \|F(x_i, p) - y_i\|^2 \quad (5.3)$$

The regression was done again using different weighs, the logarithm model and for an elevation in the range 80 - 90. The results are presented at the table 5.6. Automatic means that the weights are chosen by intervals of the wind as the number of points in this interval. This allow to re-equilibrate the histogram of the wind. The interval chosen are [0, 2, 4, 5, 6, 7, 8, 9, 10, 14, 15, 30].

| Weights | U10 <15 | | U10 >15 | |
|------------------|---------|----------|---------|----------|
| | Bias | Variance | Bias | Variance |
| w(U10 >10) = 1 | | | | |
| w(U10 >12) = 0.8 | 1.5080 | 7.1320 | -4.6708 | 2.7809 |
| w(U10 >15) = 0.5 | | | | |
| w(U10 >10) = 0.6 | | | | |
| w(U10 >12) = 0.4 | 5.0018 | 7.1774 | -1.3445 | 2.4296 |
| w(U10 >15) = 0.1 | | | | |
| Auto | 0.5162 | 7.6284 | -5.4330 | 4.0698 |

Table 5.6: Results of regression with weights

The result of the regression on the test set for the range of elevation [70-90] is presented as well in figure 5.13.

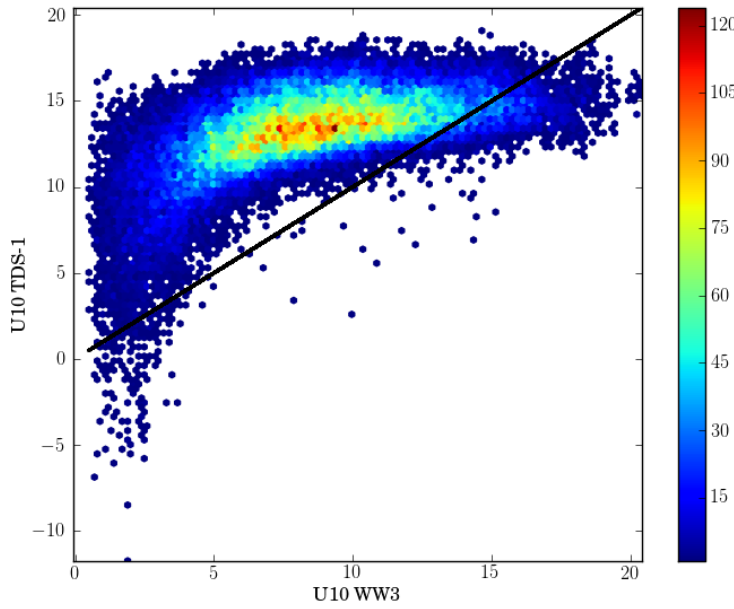


Figure 5.13: Weighted regression $w(U10 > 10) = 0.6$ $w(U10 > 12) = 0.4$ $w(U10 > 15) = 0.1$

The results are better for high winds as the bias has diminished for the different cases. But the global inversion is impacted and the bias for low wind increase. It seems that even with the weights, the problem of the SNR that saturates is limiting the capabilities of retrieving high winds. A supplementary information is needed if we are to keep the global performances and improve the high-wind retrieval.

If we suppose that we have access to the SWH by other means, the result can be improved in some cases. The figure 5.14 presents the results obtained previously and add an information about the SWH taken from WW3. It can be seen that for low winds, the wind obtained is dependent on the SWH. At high winds, although the separability is lower, high SWH appears which were not present at low wind. This gives the idea to regressions by range of SWH to improve results.

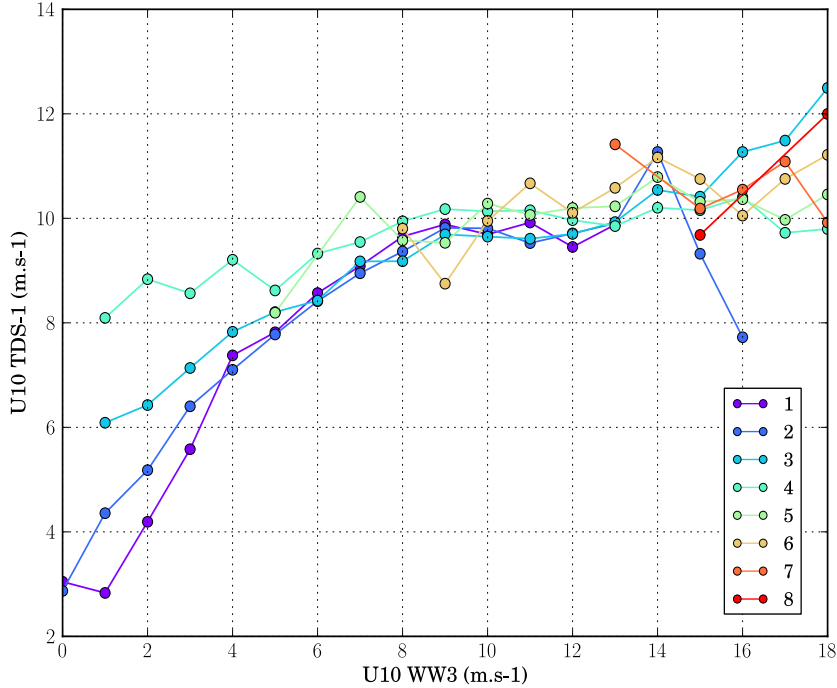


Figure 5.14: U10 TDS-1 vs U10 WW3 by range of SWH (m)

By using the SWH provided by WW3, the regression can be done by range of SWH. The results are presented in table 5.7.

| Range SWH (m) | Bias | Variance | Number of points |
|---------------|-----------|----------|------------------|
| 1 - 3 | -7.518357 | 1.413229 | 15 |
| 4 - 6 | -4.7806 | 1.9152 | 1203 |
| 7 - 9 | -1.4997 | 1.1335 | 554 |

 Table 5.7: Results by range of SWH and considering points for which $U10 > 15m.s^{-1}$

The range of SWH between 1 and 3 is not significant as the number of points is low. The range 4 - 6 have similar performances than previous regressions when trying to retrieve high winds. The interesting case is for a range of 7 - 9. Indeed, we can see an improvement of the bias as this range represent high-waves, which are mostly correlated to high-winds. The regression takes then into account solely this particular regime into account resulting in an improvement.

5.5.4 Favourable case

The precedent study considers the capabilities of retrieval for a global coverage in most of the cases. We can consequentially improve results by limiting the study to the most favourable cases where there is no saturation. This approach is used in [Foti et al., 2015].

Data is filtered in order to keep the points corresponding to $SNR > 0dB$ with a range of elevation of [80 - 90]. The threshold used in [Foti et al., 2015] is 3dB, but the number of points remaining in our case is very low so it was lowered. We have then at disposition about 4000 points.

| Model | U10 <10 | U10 >10 |
|-------------|-------------------|-------------------|
| exponential | Biais = 0.6489 | Biais = -2.9759 |
| | Variance = 3.1329 | Variance = 4.3788 |
| logarithm | Biais = 0.8405 | Biais = -3.3897 |
| | Variance = 3.3232 | Variance = 3.5633 |

Table 5.8: Results of the regression in a Favourable case

Results of the regression with no weights for both the exponential and logarithm model are presented in table 5.8. As wind available are generally not as high as the previously for this case, the threshold chosen for high winds is lowered to 10m.s^{-1} . The figure 5.15 gives the results of the regression on the test set for the exponential model.

The results are much better for low winds, which is to be expected given the shape of the curve in figure 5.8 for high SNR and low winds.

The high winds are no better by the fact that they are not really numerous in the dataset. The logarithm model saturates at lower winds (10m.s^{-1}) than the exponential one (12m.s^{-1}). It is then less efficient.

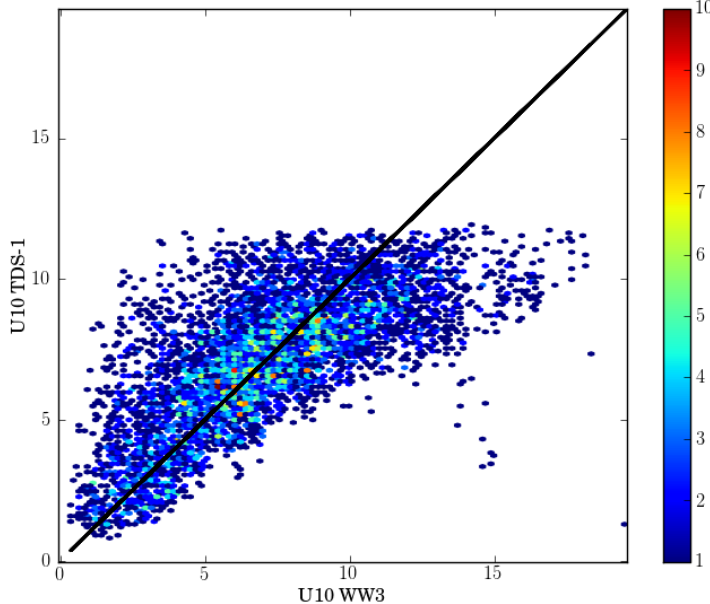


Figure 5.15: Exponential regression Favourable case

Using the same method as previously, weights were put in order to improve the results for high winds. The weights chosen for both models are $w(U10 > 10] = 0.8$, $w(U10 > 12) = 0.7$, $w(U10 > 14) = 0.3$.

The table 5.9, and the figure 5.16 give the results. It appears that the bias for high winds are improved for both winds compared to the non weighted regressions.

The performances are lower than the precedent study for high winds, as the dataset does not contain a consequent population of these points. What is interesting here, is that the global performances are far better than any other case seen this far. Especially for the exponential case in figure 5.16, where we have an interesting dynamic of wind up to $15m.s^{-1}$ and good global performances.

This last GMF developed in this study appears to be a very good starting point for ocean wind inversion at a global scale, with a similar performance to the one presented by [Foti et al., 2015].

| Model | U10 <10 | U10 >10 |
|-------------|---------------------|---------------------|
| exponential | Biais = 1.1033 | Biais = -0.9413 |
| | Variance = 4.6436 | Variance = 5.6167 |
| logarithm | Biais = 2.011227 | Biais = -1.567768 |
| | Variance = 4.918674 | Variance = 4.095104 |

Table 5.9: Results of the regression in a Favourable case with weights

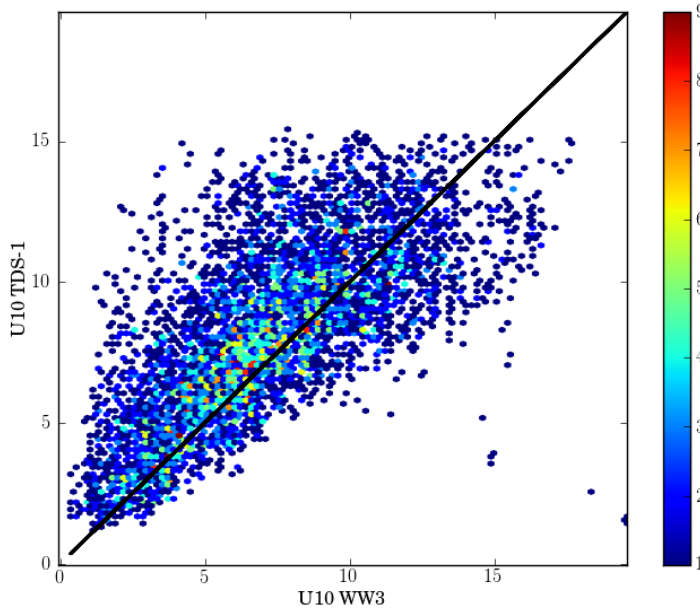


Figure 5.16: Exponential regression Favourable case and weights

Conclusions

In this thesis, we explored the capabilities of the GNSS-R technique for the wind retrieval. The work was based on the mission TechDemoSat-1 which provided an important dataset for the study.

The first chapter developed the theory behind this novel type of Remote Sensing. It presented the physical assumptions, as well as the processing techniques in order to obtain the Waveforms which are used in order to retrieve geophysical information. The second chapter described the dataset, which is consequent and has a global coverage. It also showed that the initial object of the study, the storms, could not be achieved as no significant data is available. We then developed a model for the waveforms and explored the different sensitivities to the wind. This led to the chapter 5, where the SNR was used as a parameter in order to invert the dataset through a transfer function obtained by regressions. The results are good for moderate winds but the saturation of the SNR for high winds led to an important bias. Several methods to improve the results were explored. The use of weights can improve the results for high winds but decrease them for lower winds. The use of information about SWH can also improve the results at high winds. Finally, a favourable case where a good GMF is obtained for all winds up to $15m.s^{-1}$ was presented. This last results compares to the ones presented in the literature for the inversion of TechDemoSat-1 data.

As this study was limited by the datasets used, it would be interesting to explore different ones. Crossing with different storms dataset, in peculiar with Atlantic and non tropical storms, could be interesting. Another step can be using the ASCAT wind obtained directly from the satellite and not daily map for the regressions.

The results of the study were limited partly because of the Automatic Gain mode. If the information about the gain is released in the future, it would be promising to use the direct model described in Chapter 4, in order to retrieve wind information.

Bibliography

- [Amarouche, 2001] Amarouche, L. (2001). *Contribution à l'Etude du Biais d'Etat de Mer*. Phd thesis, Université Paris 7 - Denis Diderot.
- [Elfouhaily et al., 1997] Elfouhaily, T., Chapron, B., Katsaros, K., and Vandemark, D. (1997). A unified directional spectrum for long and short wind-driven waves. *Journal of Geophysical Research: Oceans*, 102(C7):15781–15796.
- [Elfouhaily et al., 2002] Elfouhaily, T., Thompson, D. R., and Linstrom, L. (2002). Delay-doppler analysis of bistatically reflected signals from the ocean surface: theory and application. *IEEE Transactions on Geoscience and Remote Sensing*, 40(3):560–573.
- [Foti et al., 2015] Foti, G., Gommenginger, C., Jales, P., Unwin, M., Shaw, A., Robertson, C., and Roselló, J. (2015). Spaceborne gnss reflectometry for ocean winds: First results from the uk techdemosat-1 mission. *Geophysical Research Letters*, 42(13):5435–5441. 2015GL064204.
- [Gleason, 2006] Gleason, S. (2006). *Remote Sensing of Ocean, Ice and Land Surfaces Using Bistatically Scattered GNSS Signals From Low Earth Orbit*. Phd thesis, University of Surrey.
- [Gleason et al., 2005] Gleason, S., Adjrad, M., and Unwin, M. (2005). Sensing ocean, ice and land reflected signals from space: results from the uk-dmc gps reflectometry experiment. In *Proceedings of the 2005 ION GNSS Technical Meeting*, pages 13–16. Citeseer.
- [Shan, 2006] Shan, S. (2006). A levenberg-marquardt method for large-scale bound-constrained nonlinear least-squares. Master thesis, Acadia University.
- [Soulat, 2003] Soulat, F. (2003). *Sea Surface Remote Sensing with GNSS and Sunlight Reflections*. Phd thesis, UPC-Starlab.
- [Stratton, 1941] Stratton, J. (1941). *Electromagnetic theory*. International series in pure and applied physics. McGraw-Hill book company, inc.
- [Zavorotny et al., 2014] Zavorotny, V. U., Gleason, S., Cardellach, E., and Camps, A. (2014). Tutorial on remote sensing using gnss bistatic radar of opportunity. *IEEE Geoscience and Remote Sensing Magazine*, 2(4):8–45.
- [Zavorotny and Voronovich, 2000] Zavorotny, V. U. and Voronovich, A. G. (2000). Scattering of gps signals from the ocean with wind remote sensing application. *IEEE Transactions on Geoscience and Remote Sensing*, 38(2):951–964.

Résumé

Ce stage s'inscrit dans le cadre des activités de la division océanographie spatiale de CLS concernant le développement d'outils de mesure de paramètres géophysiques.

Ce rapport explore les capacités de mesure d'une technique récente d'océanographie spatiale, la réflectométrie GNSS. L'étude s'appuie sur une récente mission spatiale, TechDemoSat-1 qui met à disposition une base de données de mesure.

Dans un premier temps, des outils ont été développés pour caractériser la base de données et la comparer à d'autres références. Puis une simulation de la mesure a été effectuée à l'aide de travaux récents sur la physique des interactions entre la surface océanique et les ondes électromagnétiques. À l'aide de cette simulation, différentes sensibilités au vent ont été trouvées et ont été utilisées pour développer des méthodes pour inverser les données de la mission TechDemoSat-1.

Abstract

This internship is in line with the activities of the Oceanography division of CLS concerning the development of methods to measure geophysical parameters.

This thesis explores the retrieval capabilities of a novel Remote Sensing approach known as the GNSS Reflectometry. The study is based on a recent space mission, TechDemoSat-1 which offers a consequent database.

Firstly, tools for examining and characterising the database were developed. Then a simulation of the measure has been implemented through recent works on the interaction between the ocean's surface and the electromagnetic wave. Using this simulation, sensitivities to the wind speed were found and used in order to invert the dataset of TechDemoSat-1.